# Chapter 2

# Fin-Hull Interaction: The Hydrodynamic Model

**The paper "A Numerical Model of the Flow Around Ship-Mounted Fin Stabilizers," (reference [57]), by Liut *et al.*, is based on the contents of this chapter.**

## 2.1 Introduction

In this chapter we discuss a numerical model for the flow over fins attached to the hull of a ship. We call this model FINS; it is quite general and accounts for the full six-degree-of-freedom motion of the ship as well as the hydrodynamic interference between the hull and the fins. We developed FINS in such a way that it can be combined, or used in conjunction, with other existing codes that predict ship motions and thereby extend their capabilities. To illustrate how it can be combined with an existing code, we selected the program LAMP, we mentioned in Chapter 1 (FINS can just as easily be combined with other codes).

LAMP simultaneously and interactively predicts both the flowfield around and the motion of a ship in a seaway in the time domain. LAMP uses a source distribution on the instantaneous wetted surface of the hull, a practice that requires re-paneling the ship at each time step. The flow generated by the sources satisfies the linearized free-surface condition on the incident wave. This implies that the motion of the ship creates a relatively small disturbance. However it is not assumed that the amplitudes of the motion of the ship and the waves are small. The nonlinear terms are retained in the equations of motion of the ship. Several comparisons have shown the numerical results to be in good

agreement with the experimental data. The numerical results also predict some roll instabilities excited by the pitching motion that have been observed and which are truly nonlinear phenomena.

LAMP currently does not have the capability of modeling the flowfield around and predicting the hydrodynamic forces acting on fins attached to the hull of a ship. Thus the influence of fins on the motion of the ship cannot be modeled. In this chapter we show how to extend the capabilities of LAMP (or any such code) to include fins so that, when the equations of motion are integrated, the hydrodynamic loads acting on the fins are included. The fins are modeled by a general unsteady vortex-lattice method, instead of sources. Thus, the complete simulation is based on distributions of sources and vorticity. In addition, the problem is somewhat complicated by the fact that the grids needed to produce accurate estimates of the loads on the ship can be much coarser than those needed to produce accurate estimates of the forces acting on the fins. Different meshes require different time steps. As a result, the complete simulation consists of two interacting programs running different meshes with different singularities and different time steps.

The vortex-lattice modeling in FINS is performed by a lattice of discrete vortex lines. It computes the distribution of vorticity in and the location of the wakes generated by the fins as part of the solution. The model includes the portions of the hull in the neighborhoods of the fins and their wakes. These “portions” are arbitrary and could even include the entire hull. The model accounts for the hydrodynamic interference between the ship and the fins when the loads on the fins are calculated. LAMP does not take the fins into account when the hydrodynamic loads on the hull are calculated, the assumption being that the fins disturb only a small portion of the entire flowfield around the hull. FINS does not model the free surface, either, the assumption being that the fins are attached near the bottom of the hull and can be considered deeply submerged. These assumptions fit an important class of applications. Though more expensive from a

computational standpoint, FINS can take into account the influence of the waves computed by LAMP (or any other such code).

The motion of the fins can be completely general as long as the effective angle of attack is not large enough to induce either separation or cavitation. The fins can also move with respect to the hull. Furthermore, FINS can model the fins with movable flaps. These features can be used for active control as discussed in Chapters 5, 8 and 9.

In what follows, we first describe FINS and then the procedure for combining FINS and LAMP. Next we present some numerical experimental results. Finally we give some closing comments.

## 2.2 FINS

The boundary layers on the fins and hull, as well as the wakes emanating from the tips and trailing edges of the fins, are relatively thin layers of very concentrated vorticity. Vorticity, $\boldsymbol{\Omega}$, is defined as follows:

$$\boldsymbol{\Omega}(\mathbf{r},t) = \nabla \times \mathbf{v}(\mathbf{r},t) \tag{2.1}$$

where $\mathbf{v}$ is the fluid velocity at position $\mathbf{r}$ and time $t$, and $\nabla$ is the vector operator that has the following familiar form in a rectangular Cartesian coordinate system:

$$\nabla = \mathbf{i}\frac{\partial}{\partial x} + \mathbf{j}\frac{\partial}{\partial y} + \mathbf{k}\frac{\partial}{\partial z} \tag{2.2}$$

The continuity equation for an incompressible fluid is

$$\nabla \cdot \mathbf{v} = 0 \tag{2.3}$$

Equations (2.1) through (2.3) can be manipulated to express the velocity as a function of vorticity (see, *e.g.*, Karamcheti [40]) :

$$\mathbf{v}(\mathbf{r},t)=\frac{1}{4\pi}\iiint_{\Lambda(t)}\frac{\boldsymbol{\Omega}(\boldsymbol{\eta},t)\times(\mathbf{r}-\boldsymbol{\eta})}{|\mathbf{r}-\boldsymbol{\eta}|^2}\,d\Lambda(\boldsymbol{\eta}) \tag{2.4}$$

where $\Lambda$ is the volume of the flowfield and $\boldsymbol{\eta}$ is the position vector used as the variable of integration. It follows from equation (2.4) that vorticity anywhere is associated with velocity everywhere in the fluid. Equation (2.4) is a kinematic result; hence, it is valid for *viscous* as well as *inviscid* fluids.

In the real flow, the velocity associated with the vorticity in the boundary layers (fins and hull) disturbs the flowfield in such a way that the boundary conditions are satisfied. In the numerical model of the flow, we imitate this phenomenon by requiring the velocity associated with $\boldsymbol{\Omega}$ to satisfy the no-penetration boundary condition:

$$[\mathbf{v}_B(\mathbf{r},t)+\mathbf{v}_W(\mathbf{r},t)+\mathbf{v}_M(\mathbf{r},t)+\mathbf{v}_R(\mathbf{r},t)-\mathbf{v}_S(\mathbf{r},t)]\cdot\mathbf{n}(\mathbf{r},t)=0 \tag{2.5}$$

where $\mathbf{v}_B$ is the velocity associated with the vorticity in the boundary layers on the structure, $\mathbf{v}_W$ is the velocity associated with the vorticity in the wake, $\mathbf{v}_M$ is the freestream velocity, $\mathbf{v}_R$ is the velocity associated with the free surface, $\mathbf{v}_S$ is the velocity of the structure, and $\mathbf{n}$ is a vector normal to the surface of the structure. By structure we mean the ship hull and the fins. Using equation (2.4) we can rewrite equation (2.5) as follows:

$$[\mathbf{v}_S-\mathbf{v}_W-\mathbf{v}_M-\mathbf{v}_R]\cdot\mathbf{n}=\frac{1}{4\pi}\left[\iiint_{\Lambda'}\frac{[\boldsymbol{\Omega}\times(\mathbf{r}-\boldsymbol{\eta})]}{|\mathbf{r}-\boldsymbol{\eta}|^2}\,d\Lambda(\boldsymbol{\eta})\right]\cdot\mathbf{n} \tag{2.6}$$

where Λ' is the sub-volume of the flowfield that includes only the boundary layers. In practice the boundary conditions are satisfied at certain control points. This is described later. The velocity of the structure, $\mathbf{v}_S(t)$, is given by

$$\mathbf{v}_S(\mathbf{r},t) = \mathbf{v}_O(t) + \boldsymbol{\omega}(t) \times \boldsymbol{\rho} + \mathbf{v}_F(\mathbf{r},t) \tag{2.7}$$

where $\mathbf{v}_O(t)$ is the translational velocity of the ship, $\boldsymbol{\omega}(t)$ is the angular velocity of the ship with respect to a ground-fixed frame of reference, $\boldsymbol{\rho}$ is the position of any point $P$ on the fins with respect to a ship-fixed frame of reference and $\mathbf{v}_F(\mathbf{r},t)$ is the velocity produced by the angular rotation of the fins with respect to the ship and the angular rotation of the flaps relative to fins. This is described in more detail in section 2.4.

Equation (2.6), which holds everywhere on the wetted surface of the structure, must be solved for $\boldsymbol{\Omega}$. A convenient way to express the integral in equation (2.6) approximately in terms of $\boldsymbol{\Omega}$ is to replace the continuous vortex sheet with a lattice of discrete vortex lines. Such a lattice is shown in Figure 2-1. It has 35 elements and 48 nodes (nodes are shown as $\bullet$). The lines in this figure represent straight, discrete vortex segments. Similar latices are used to approximate the boundary layers on the hull near the fins and to represent the wakes emanating from the tips and trailing edges of the fins.

When the vorticity is confined to a finite-length straight segment, equation (2.4) reduces to the following (see, *e.g.*, Katz and Plotkin [44]):

$$\mathbf{v}_{12} = \frac{\Gamma(\mathbf{r}_{12} \times \mathbf{r}_{1P})}{4\pi |\mathbf{r}_{12}|^2 \, h} \left[ \left( \frac{\mathbf{r}_{1P}}{|\mathbf{r}_{1P}|} - \frac{\mathbf{r}_{2P}}{|\mathbf{r}_{2P}|} \right) \cdot \mathbf{r}_{12} \right] \tag{2.8}$$

whose module can be computed as:

$$|\mathbf{v}_{12}| = \frac{\Gamma(t)}{4\pi h} \left[ \cos\beta_1 - \cos\beta_2 \right] \tag{2.9}$$

Here $\Gamma$ is the circulation around the vortex segment (average value of $\boldsymbol{\Omega}$ times the cross sectional area of the segment) and $h$ is the distance from this segment to the point in the flowfield where the velocity associated with the vorticty segment is computed. The remaining variables in equations (2.8) and (2.9) are defined in Figure 2-2. In this figure, the vortex segment runs from points **1** to **2**. Equation (2.8) is known as the Biot-Savart Law. It is essentially the same law first discovered to compute magnetic fields associated with an electric current (1820).

Though the fins have thickness, in FINS the boundary layers on the upper and lower surfaces are merged into a single vortex sheet called a lifting surface. In our case the fins have symmetric profiles, so the lifting surface is flat. Comparisons with experiments prove this to be a reasonable simplification.

Kelvin-Helmholtz Theorem of spatial conservation of circulation states that at any instant the circulation around any cross sectional area of a vortex tube (or filament) remains constant. A consequence of this is that vortex lines can neither begin nor end in the flowfield. In a lattice of vortex lines this requires that at any node, the sum of all circulations be zero. Each element $e$ of the lattice (which constitutes a close circuit of vortex segments) has a circulation $G_e(t)$ associated with it. This circulation is given along a close ring of vorticity, which extends along the boundaries of every element. An example of such lattice was shown in Figure 2-1. The circulations around the segments between two nodes on the mesh are the differences between the closed-loop circulations for two adjoining elements. Therefore the sum of the circulations coming to any node is zero for all time, in consonance with the principle that vortex lines can neither begin nor end in the flowfield. Thus for example, referring again to Figure 2-1, the circulation between nodes **2** and **10** are given by $\Gamma_{2-10} = G_6 - G_1$, and at node **10** the sum of all circulations are zero $\left(\Gamma_{2-10} + \Gamma_{10-18} + \Gamma_{10-9} + \Gamma_{11-10} = 0\right)$.

Because we have discretized the lifting-surface vortex sheet, we can only satisfy the no-penetration condition, equation (2.5), at a finite number of points. We choose these

points to be the centroids of the corners of each element. These are called the control points.

Our first objective is to compute the circulations $G_e$ of each element $e$. Using equation (2.8), the velocity per unit of circulation associated with any segment of vorticity $\gamma$ between any two nodes $i$ and $j$ of an element $\varepsilon$, measured at the control point of a different (or the same) element $e$, can be computed by:

$$\mathbf{v}_{\gamma}^{e\varepsilon} = \mathbf{v}_{ij}^{e\varepsilon} = \frac{\left(\mathbf{r}_{ij} \times \mathbf{r}_{ie}\right)}{4\,\pi \left|\mathbf{r}_{ij}\right|^2 h_{ij}^{e\varepsilon}} \left[ \left( \frac{\mathbf{r}_{ie}}{\left|\mathbf{r}_{ie}\right|} - \frac{\mathbf{r}_{je}}{\left|\mathbf{r}_{je}\right|} \right) \cdot \mathbf{r}_{ij} \right] \tag{2.10}$$

Here $h_{ij}^{e\varepsilon}$ is the distance from any segment of vorticity $i$-$j$ of element $\varepsilon$ to the control point of element $e$. Using equation (2.10), we can define a velocity coefficient $A_{e\varepsilon}$ as

$$A_{e\varepsilon} = \sum_{\gamma=1}^{N_{\varepsilon}^{\gamma}} \mathbf{v}_{\gamma}^{e\varepsilon} \cdot \breve{\mathbf{n}}^{e} \qquad \text{for} \qquad e = 1,\ldots,\ N_B^e \tag{2.11}$$

where $N_{\varepsilon}^{\gamma}$ is the number of sides of element $\varepsilon$ (four for quadrilateral elements), $N_B^e$ is the total number of elements in the boundary layer (hull and fins), $\breve{\mathbf{n}}^{e}$ is the normal unit vector to element $e$ and $A_{e\varepsilon}$ are the velocities per circulation $G_{\varepsilon}$ normal to the control point of element $e$ induced by the close loop of the discrete vortex segments encircling each element $\varepsilon$. For the present problem, the body-fixed panels are distributed along the fins and the neighboring parts of the hull.

From equations (2.5), (2.6), (2.10), and (2.11) we obtain a system of $N_B^e$ algebraic equations, where the circulations $G_e$ are the unknowns. This can be expressed as

$$\sum_{\varepsilon=1}^{N_B^e} A_{e\varepsilon}\ G_{\varepsilon} = -\left(\mathbf{v}_S - \mathbf{v}_W - \mathbf{v}_M - \mathbf{v}_R\right)_e \cdot \breve{\mathbf{n}}^{e} \qquad \text{for} \qquad e = 1,\ldots,\ N_B^e \tag{2.12}$$

## 2.3 Kutta Condition and Shedding

When viscous effects are ignorable and pressure is continuous, it follows from the Kelvin-Helmholtz theory that

$$\frac{D\Gamma(t)}{Dt} = 0 \tag{2.13}$$

where $\Gamma$ is the circulation around a closed loop of fluid particles and $\frac{D}{Dt}$ denotes the usual substantial derivative. Equation (2.13) states that as a closed loop of particles convects in a flowfield, the circulation around that loop remains constant. This result is often called temporal conservation of circulation and is the basis for modeling the wake; it provides the rate at which vorticity is shed from the fin as well as the subsequent time-varying spatial distribution of vorticity in the wake.

As fluid flows over the fins, the pressures on the upper and lower surfaces must reach the same value along the trailing edge and fin tip (we call them shedding edges) so that the pressure is continuous in the flowfield. This is known as the Kutta Condition. We have assumed that viscous stresses are negligible in the flowfield everywhere outside the boundary layers; hence it follows that: (1) the segments along the shedding edges convect with the velocity of the local fluid particles, and (2) the circulations around these segments remain constant.

As the shedding process continues, the vortex lines that are being shed evolve into a vortex lattice. The positions of the ends of every vortex segment in the wake, in a ground-fixed reference frame, are computed according to a simple Euler algorithm:

$$\mathbf{r}(t+\Delta t) = \mathbf{r}(t) + \left\{\mathbf{v}_B\left[\mathbf{r}(t)\right] + \mathbf{v}_W\left[\mathbf{r}(t)\right] + \mathbf{v}_M\left[\mathbf{r}(t)\right]\right\}\Delta t \tag{2.14}$$

where $\Delta t$ is the time step, $\mathbf{r}(t+\Delta t)$ is the position of an end point of a given vortex segment at time $t+\Delta t$, and $\mathbf{r}(t)$ is the position of the same point at time *t*.

By convecting the entire closed loop of vortex segments from the elements along the shedding edges, we automatically satisfy the requirements of both spatial and temporal conservation of circulation in the wake. The process is illustrated in Figure 2-3. In this figure, three elements along the trailing edge are represented. The situation depicted is three time steps following an arbitrary time *t*. The numbering of elements is the same as that in Figure 2-1.

For example, the circulation around the vortex segment running from node 43 to node 44 is $\Gamma_{43-44} = G_{15}(t+2\Delta t) - G_{15}(t+3\Delta t)$, and that for the segment running from node 51 to node 52 is $\Gamma_{51-52} = G_{15}(t+\Delta t) - G_{15}(t+2\Delta t)$. At time $= t+3\Delta t$, the circulation around the segment between nodes 43 and 44 is $\Gamma_{43\text{-}44}$, at time $= t+2\Delta t$ it was $\Gamma_{51\text{-}52}$, *etc*. In a similar way, one can obtain the rest of the circulations. A two-dimensional view of this process is displayed in Figures 2-4 and 2-5.

On every element on the wake the following remains valid:

$$G_e = \sum_{i=1}^{N_e^\gamma} \Gamma_{e_i} \qquad \text{for} \quad e = 1,\ldots,\ N_w^e \tag{2.15}$$

and

$$\sum_{j=1}^{N_n^\gamma} \Gamma_j = 0 \qquad \text{for} \quad n = 1,\ldots,\ N_w^n \tag{2.16}$$

where $N_e^\gamma$ is the number of vortex segments (or nodes) of element *e*, $N_w^e$ is the number of elements in the wake vortex lattice, $N_n^\gamma$ is the number of vortex segments concurring

at node *n*, and $N_w^n$ is the number of nodes in the wake vortex lattice. For quadrilateral elements $N_e^\gamma = N_n^\gamma = 4$.

So far we have found a way to compute the circulations around the vortex segments enclosing each of the elements of the fin at every time step. Our final goal is to determine the lift and moments generated by each fin at every time step. Away from the vortex sheets the flow is irrotational; therefore in these regions Bernoulli's equation can be used to determine the pressure that is being generated on each of the elements of the fin. The hydrodynamic force exerted on each element is equal to the product of its area, the difference in the pressures on the upper and lower sides of the surface at the control point, and the unit vector normal to the surface. The computation of these forces is the subject of the next section.

## 2.4 Pressure Computations

A familiar form of Bernoulli's equation is given by

$$\frac{\partial \Phi(\mathbf{r},t)}{\partial t} + \frac{\mathbf{v}(\mathbf{r},t)\cdot\mathbf{v}(\mathbf{r},t)}{2} + g\,z + \frac{p(\mathbf{r},t)}{\rho} = \frac{\mathbf{v}_c\cdot\mathbf{v}_c}{2} + g\,z_c + \frac{p_c}{\rho} \tag{2.17}$$

where **v** is the velocity of the fluid, Φ is the velocity potential, *p* is the pressure of the fluid, ρ is the density of the fluid (constant), *z* is the depth, and *g* is the acceleration of gravity. The subscripts *c* on the right-hand side designate characteristic parameters. The position vector **r** is given in a ground-fixed reference frame or *G*-frame.

We can use equation (2.17) to write the following expressions for the pressure on the upper and lower sides of a lifting surface:

$$p_u - p_c = \frac{1}{2}\rho\left(\mathbf{v}_c\cdot\mathbf{v}_c - \mathbf{v}_u\cdot\mathbf{v}_u\right) + \rho\, g\left(z_c - z_u\right) - \frac{\partial\Phi}{\partial t} \tag{2.18}$$

$$p_l - p_c = \frac{1}{2}\rho\left(\mathbf{v}_c \cdot \mathbf{v}_c - \mathbf{v}_l \cdot \mathbf{v}_l\right) + \rho\, g\left(z_c - z_l\right) - \frac{\partial \Phi}{\partial t} \tag{2.19}$$

where the subscripts *u* and *l* stand for the upper and lower sides, respectively.

In determining the hydrodynamic forces we calculate the difference in the pressures $\Delta p$ above and below at the control points of each element; so $p_u$ and $p_l$ are the pressures just above and below any control point. Subtracting (2.18) from (2.19) and rearranging terms, we get:

$$\Delta p = p_l - p_u = \frac{1}{2}\rho\left(\left(\mathbf{v}_u + \mathbf{v}_l\right)\cdot\left(\mathbf{v}_u - \mathbf{v}_l\right) + 2\,\frac{\partial(\Phi_u - \Phi_l)}{\partial t}\right) \tag{2.20}$$

The terms containing *z* in equations (2.18) and (2.19) produce the buoyant force, which is neglected (for our zero-thickness fin model it is exactly zero).

Next we describe how to compute $\frac{\partial(\Phi_u - \Phi_l)}{\partial t}$ and $\left(\mathbf{v}_u - \mathbf{v}_l\right)$. We start with the partial derivative of $\Phi$ with respect to *t*. This derivative must be calculated at a given position in the *G*-frame. Such a derivative is somewhat difficult to compute directly, but we can express it in terms of the derivative of $\Phi$ at a fixed point on the moving lifting surface, which is rather easy to compute. To connect the derivative of $\Phi$ in the *G*-frame with the corresponding derivative of $\Phi$ referred to the lifting surface, we begin with the following Taylor Series:

$$\Phi(\mathbf{r} + \Delta\mathbf{r}, t + \Delta t) = \Phi(\mathbf{r}, t) + \nabla\Phi(\mathbf{r}, t)\cdot\Delta\mathbf{r} + \frac{\partial \Phi}{\partial t}(\mathbf{r}, t)\,\Delta t + HOT \tag{2.21}$$

where the acronym *HOT* stands for higher order terms in $\Delta t$ and $\Delta\mathbf{r}$. Rearranging terms in equation (2.21) and dividing both sides by the time increment $\Delta t$ yields the following

$$\frac{\partial \Phi(\mathbf{r},t)}{\partial t} = \frac{\Phi(\mathbf{r}+\Delta\mathbf{r},t+\Delta t)-\Phi(\mathbf{r},t)}{\Delta t} - \nabla\Phi(\mathbf{r},t)\cdot\frac{\Delta\mathbf{r}}{\Delta t} + HOT \tag{2.22}$$

The variables **r** and *t* are independent and may be specified arbitrarily. We choose the vector $\Delta\mathbf{r}$ in such a way that it follows a selected point *P* fixed on the lifting surface during the time increment $\Delta t$; that is, we make $\Delta\mathbf{r}$ be the displacement of *P*. Therefore, when we take the limit as $\Delta t \to 0$, we get

$$\lim_{\Delta t\to 0}\left(\frac{\Delta\mathbf{r}}{\Delta t}\right) = \mathbf{v}_P \tag{2.23}$$

and

$$\lim_{\Delta t\to 0}\left(\frac{\Phi(\mathbf{r}+\Delta\mathbf{r},t+\Delta t)-\Phi(\mathbf{r},t)}{\Delta t}\right) = \left.\frac{D\Phi(\mathbf{r},t)}{Dt}\right|_P \tag{2.24}$$

where $\mathbf{v}_P$ is the velocity of point *P*, and the derivative operator $\frac{D}{Dt}$ stands for the substantial derivative following point *P* on the lifting surface. Then it follows that

$$\left.\frac{\partial \Phi(\mathbf{r},t)}{\partial t}\right|_{\mathbf{r}=\mathbf{r}_P} = \left.\frac{D\Phi}{Dt}\right|_P - \nabla\Phi\big|_{\mathbf{r}=\mathbf{r}_P}\cdot\,\mathbf{v}_P \tag{2.25}$$

where $\mathbf{r}_P$ is the position of point *P* (fixed to the fin) with respect to the *G*-frame.

Let's now compute the velocity $\mathbf{v}_P$. The position vector $\mathbf{r}_P = {}^G\mathbf{r}^P$ between a point *P* on the fin and the origin of the *G*-frame can be expressed as

$${}^G\mathbf{r}(t)^P = {}^G\mathbf{r}(t)^B + {}^B\mathbf{r}^F + {}^F\mathbf{r}(t)^P \tag{2.26}$$

where ${}^{G}\mathbf{r}^{B}$ is the position of the body-fixed frame of reference (we call this the *B*-frame; see Figure 2-6) with respect to the *G*-frame, ${}^{B}\mathbf{r}^{F}$ connects the origin of a frame fixed to the fin (*F*-frame) to the origin of the *B*-frame, and ${}^{F}\mathbf{r}^{P}$ is the position of point *P* in the *F*-frame. When we take the limit of $\mathbf{r}_P$ as $\Delta t \to 0$ [equation (2.23)], the derivative of $\mathbf{r}_P$ with respect to *t* yields the absolute velocity $\mathbf{v}_P = {}^{G}\mathbf{v}^{P}$ of point *P*:

$$ {}^{G}\mathbf{v}^{P} = {}^{G}\mathbf{v}^{B} + {}^{G}\boldsymbol{\omega}^{B} \times {}^{B}\mathbf{r}^{F} + {}^{F}\mathbf{v}^{P} + {}^{G}\boldsymbol{\omega}^{B} \times {}^{F}\mathbf{r}^{P} \tag{2.27} $$

where ${}^{G}\mathbf{v}^{B} = \dfrac{\partial {}^{G}\mathbf{r}^{B}}{\partial t}$, ${}^{G}\boldsymbol{\omega}^{B} \times {}^{B}\mathbf{r}^{F} = \dfrac{\partial {}^{B}\mathbf{r}^{F}}{\partial t}$ (${}^{B}\mathbf{r}^{F}$ is constant for an ideally inelastic ship) and ${}^{F}\mathbf{v}^{P} + {}^{G}\boldsymbol{\omega}^{B} \times {}^{F}\mathbf{r}^{P} = \dfrac{\partial {}^{F}\mathbf{r}^{P}}{\partial t}$. Since ${}^{B}\mathbf{r}^{P} = {}^{B}\mathbf{r}^{F} + {}^{F}\mathbf{r}^{P}$, then

$$ {}^{G}\mathbf{v}^{P} = {}^{G}\mathbf{v}^{B} + {}^{G}\boldsymbol{\omega}^{B} \times {}^{B}\mathbf{r}^{P} + {}^{F}\mathbf{v}^{P} \tag{2.28} $$

For the most general case when point *P* belongs to the flap, the velocity ${}^{F}\mathbf{v}^{P} = \dfrac{\partial}{\partial t}\left({}^{F}\mathbf{r}^{L} + {}^{L}\mathbf{r}^{P}\right)$ of point *P* is given by

$$ {}^{F}\mathbf{v}^{P} = {}^{B}\boldsymbol{\omega}^{F} \times {}^{F}\mathbf{r}^{L} + {}^{B}\boldsymbol{\omega}^{F} \times {}^{L}\mathbf{r}^{P} + {}^{F}\boldsymbol{\omega}^{L} \times {}^{L}\mathbf{r}^{P} \tag{2.29} $$

where ${}^{B}\boldsymbol{\omega}^{F}$ is the angular velocity of the *F*-frame with respect to the *B*-frame, ${}^{F}\boldsymbol{\omega}^{L}$ is the angular velocity of a frame fixed to flap (*L*-frame) with respect to the *F*-frame, ${}^{B}\boldsymbol{\omega}^{F} \times {}^{F}\mathbf{r}^{L} = \dfrac{\partial {}^{F}\mathbf{r}^{L}}{\partial t}$ (${}^{F}\mathbf{r}^{L}$ is a constant for ideally inelastic fins) and ${}^{B}\boldsymbol{\omega}^{F} \times {}^{L}\mathbf{r}^{P} + {}^{F}\boldsymbol{\omega}^{L} \times {}^{L}\mathbf{r}^{P} = \dfrac{\partial {}^{L}\mathbf{r}^{P}}{\partial t}$. Since ${}^{F}\mathbf{r}^{P} = {}^{F}\mathbf{r}^{L} + {}^{L}\mathbf{r}^{P}$ (see Figure 2-6), then

$$ {}^{F}\mathbf{v}^{P} = {}^{B}\boldsymbol{\omega}^{F} \times {}^{F}\mathbf{r}^{P} + {}^{F}\boldsymbol{\omega}^{L} \times {}^{L}\mathbf{r}^{P} \tag{2.30} $$

For this analysis the origin of the *F*-frame and the *L*-frame must contain ${}^{B}\boldsymbol{\omega}^{F}$ and ${}^{F}\boldsymbol{\omega}^{L}$ respectively. The first term on the right hand side of equation (2.30) is valid for any point *P* on the fin, including the flap, whereas the second term only appears when point *P* belongs to the flap and ${}^{F}\boldsymbol{\omega}^{L} \neq 0$ (*e.g.*, for active-flap control applications).

We can rewrite equation (2.28) as:

$$ {}^{G}\mathbf{v}^{P} = {}^{G}\mathbf{v}^{B} + {}^{G}\boldsymbol{\omega}^{B} \times {}^{B}\mathbf{r}^{P} + {}^{F}\mathbf{v}^{P} \tag{2.31} $$

where $\mathbf{b} = {}^{B}\mathbf{r}^{P}$ is the vector connecting point *P* on the fin with the origin of the *B*-frame, $\boldsymbol{\omega} = {}^{G}\boldsymbol{\omega}^{B}$ is the angular velocity of the *B*-frame with respect to the *G*-frame, $\mathbf{v}_{O} = {}^{G}\mathbf{v}^{B}$ is the velocity of the origin of the *B*-frame with respect to the *G*-frame, and $\mathbf{v}_{F} = {}^{F}\mathbf{v}^{P}$ is the velocity of point *P* with respect to the *B*-frame.

Inserting equation (2.31) into equation (2.25) we obtain

$$ \left.\frac{\partial \Phi(\mathbf{r},t)}{\partial t}\right|_{\mathbf{r}=\mathbf{r}_P} = \left.\frac{D\Phi(t)}{Dt}\right|_{P} - \mathbf{v}(\mathbf{r}_P,t) \cdot \left(\mathbf{v}_O(t) + \boldsymbol{\omega}(t) \times \mathbf{b} + \mathbf{v}_F\right) \tag{2.32} $$

where $\mathbf{v}(\mathbf{r}_P,t) = \nabla\Phi\big|_{\mathbf{r}=\mathbf{r}_P}$ is the velocity of the fluid next to point *P* on the fin.

The potential $\Phi_u^P$ can be computed as

$$ \Phi_u^P = \Phi_l^P + \oint_{C_P} \mathbf{v} \cdot d\mathbf{r} \tag{2.33} $$

where the path of integration $C_P$ connects points in the flow just off the upper and lower surfaces of the fin associated with any control point *P* on the fin. We choose this path to

go around the leading edge, as shown in Figure 2-7. Then it follows from Stokes' theorem that the integral in equation (2.33) can be computed as

$$\phi_u - \phi_l = \oint_{C_P} \mathbf{v} \cdot d\mathbf{r} = \sum_i^{N_P^e} \Gamma_i \tag{2.34}$$

where $\Gamma_i$ are the circulations associated with the segments of vorticity, the curve $C_P$ encircles the lifting surface from a point just below $P$ to a point just above $P$, and $N_P$ is the number of such segments encircled by $C_P$ (four in Figure 2-7). Since each segment of vorticity $\Gamma_i$ can be computed as the difference between the circulations $G_j$ and $G_{j-1}$ of the two elements adjoining the vortex segment having circulation $\Gamma_i$, the sum on the right hand side of equation (2.34) is given by

$$\sum_i^{N_P} \Gamma_i = G_P \tag{2.35}$$

where $G_P$ is the circulation for the element that contains point $P$. This allows us to approximate the partial derivative of $\Phi$ with respect to $t$ in equation (2.20) as follows:

$$\frac{D\left(\Phi_u^P - \Phi_l^P\right)}{Dt} \cong \frac{G_P(t) - G_P(t-\Delta t)}{\Delta t} \tag{2.36}$$

Substituting this expression into equation (2.32), for each element $e$ we get,

$$\left.\frac{\partial\left(\Phi_u - \Phi_l\right)}{\partial t}\right|_e \cong \frac{G_e(t) - G_e(t-\Delta t)}{\Delta t} - \left(\mathbf{v}_u - \mathbf{v}_l\right)_e \cdot \left(\mathbf{v}_O(t) + \boldsymbol{\omega}(t) \times \mathbf{b}^e + \mathbf{v}_F^e\right) \tag{2.37}$$

Having found a suitable way to compute $\frac{\partial(\Phi_u - \Phi_l)}{\partial t}$, we next turn our attention to $(\mathbf{v}_u - \mathbf{v}_l)$.

In simplifying the evaluation of the integral in equation (2.6), we converted a continuous distribution of vorticity over the lifting surface into a lattice of discrete vortex segments. Now, as the first step in evaluating $\Delta\mathbf{v} = \mathbf{v}_u - \mathbf{v}_l$, we want to reverse this process and obtain the distributed vorticity. In Figure 2-8 part *a*, the area *ABCD* represents a cross section of the vortex sheet that includes a vortex segment running in the direction perpendicular to the area. The circulation around the edges of *ABCD* can be expressed as follows:

$$\Gamma = \oint_{ABCD} \mathbf{v} \cdot d\mathbf{r} \cong \Delta v \;\; \Delta l \tag{2.38}$$

where $\Delta v = |\mathbf{v}_u - \mathbf{v}_l|$. We can capture the vector properties of this relationship with the following expression:

$$\Delta\mathbf{v} = -\frac{\Gamma}{\Delta l}\left(\frac{\hat{\mathbf{n}} \times \mathbf{l}_V}{l_V}\right) \tag{2.39}$$

where $\hat{\mathbf{n}}$ is the unit vector normal to the element, $\mathbf{l}_V$ is the vector along the length of the vortex segment, and $l_V$ is its length. We view $\Gamma\,\mathbf{l}_V$ as a measure of the vorticity associated with the area *ABCD*. We generalize this expression by first introducing the following measure of the vorticity at the control point of each element (see Figure 2-8 part *b*):

$$\overline{\mathbf{\Omega}} = \frac{1}{2}\left(f_1\,\Gamma_1\,\mathbf{l}_{PQ} + f_2\,\Gamma_2\,\mathbf{l}_{QR} + f_3\,\Gamma_3\,\mathbf{l}_{RS} + f_4\,\Gamma_4\,\mathbf{l}_{SP}\right) \tag{2.40}$$

where $f_i = 1$ (for $i = 1,\ldots,4$) unless the segment lies along the leading edge in which case the $f_i$ for that segment is equal to two ( $f_i = 2$ ). Here $\mathbf{l}_{PQ}, \mathbf{l}_{QR}, \mathbf{l}_{RS}$ and $\mathbf{l}_{SP}$ are the $\mathbf{l}_V$ of equation (2.39) for the individual segments encircling the element. Then for each element it follows that

$$\Delta\mathbf{v} = \mathbf{v}_u - \mathbf{v}_l = -\frac{\hat{\mathbf{n}} \times \overline{\boldsymbol{\Omega}}}{A} \tag{2.41}$$

where $A \cong \left| \mathbf{l}_{PQ} \times \mathbf{l}_{PS} \right|$ approximates the area of the element.

Now we have obtained a suitable way to compute $\Delta\mathbf{v}$. This, and the expressions for $\frac{\partial(\Phi_u - \Phi_l)}{\partial t}$ provide all that we need to calculate the pressure jump.

Substituting equations (2.37) and (2.41) into equation (2.20) we get the following expression for the pressure jump across the lifting surface of element *e* :

$$\Delta p_e = \frac{1}{2}\rho \left( \begin{array}{l} -\left(\mathbf{v}_u + \mathbf{v}_l\right) \cdot \left( \dfrac{\hat{\mathbf{n}} \times \overline{\boldsymbol{\Omega}}}{A} \right) + 2\,\dfrac{G(t) - G(t-\Delta t)}{\Delta t} \\ -2\ \mathbf{v}_u \left(\mathbf{v}_O + \boldsymbol{\omega} \times \mathbf{b} + \mathbf{v}_F\right)_u \\ +2\ \mathbf{v}_l \left(\mathbf{v}_O + \boldsymbol{\omega} \times \mathbf{b} + \mathbf{v}_F\right)_l \\ \end{array} \right)_e \tag{2.42}$$

At any point and time, the components of $\mathbf{v}_O(t)$ and $\boldsymbol{\omega}(t) \times \mathbf{b}$ on the upper and lower surfaces of the fin are the same. Thus (2.42) reduces to:

$$\Delta p_e = \rho \left( \left[ \left(\mathbf{v}_O + \boldsymbol{\omega} \times \mathbf{b} + \mathbf{v}_F\right) - \mathbf{v}_{Mean} \right]_e \cdot \left( \frac{\hat{\mathbf{n}} \times \overline{\boldsymbol{\Omega}}}{A} \right)_e + \frac{G_e(t) - G_e(t-\Delta t)}{\Delta t} \right) \tag{2.43}$$

where $\mathbf{v}_{Mean} = \frac{1}{2}\left(\mathbf{v}_u + \mathbf{v}_l\right)$.

The resultant force on each fin can then be computed as

$$\mathbf{L} = \sum_{e=1}^{N_{Fin}^e} \Delta p_e \, A_e \, \hat{\mathbf{n}}_e \tag{2.44}$$

where $N_{Fin}^e$ is the total number of elements of each fin, and $\hat{\mathbf{n}}_e$ is the normal to element *e*.

The moment $\mathbf{M}_R$ of the hydrodynamic forces over the lifting surface with respect to any point *R* can be computed by

$$\mathbf{M}_R = \sum_{e=1}^{N_{Fin}^e} \Delta p_e \, A_e \left(\mathbf{r}_{R_e} \times \hat{\mathbf{n}}_e\right) \tag{2.45}$$

where $\mathbf{r}_{R_e}$ is the vector that connects the control point of each element *e* with point *R* .

## 2.5 Time-Marching Procedure

The predicted loads generated by the fins are functions of the motion of the ship, the motion of the fins relative to the ship, and the history of both motions. To calculate the hydrodynamic forces, FINS places a fine grid on the portions of the hull in the neighborhoods of the fins and their wakes, with elements of about the same size as those used on the fin grids. In general, this results in a disparity in element size between LAMP's and FINS' meshes. This can be seen in Figure 2-9. The no-penetration condition is imposed on the surfaces of the hull and the fins simultaneously and interactively, as described above. Finer grids require smaller time steps. Therefore the

calculation is set up to use different time steps for the fins and the ship. Thus for every LAMP time step, more than one time step usually takes place for the fin loads calculations and their associated wake computations (Figure 2-10). The size of each fin time step is adjusted in such a way that the ratio of the LAMP time step over the fin time step gives an integer number; this is the number of fin time steps that correspond to each LAMP time step. Since the predictor corrector solver may be iterating at the beginning of every (LAMP) time step, the original wake position for the current LAMP time step must be stored and used at every iteration. For every fin time step, the wake is convected, and the fin circulations are computed. By the end of the set of fin time steps corresponding to each LAMP time step, the pressures and loads are computed and the control routine is called, if active fins are used.

The entire time-marching procedure is summarized in Table 2-1.

## 2.6 Code Validation and Results

In this section we compare some numerical and experimental results.

In Figure 2-11 two solutions are represented for a fin in a free flow and a fin in the presence of an infinite wall. These solutions were obtained by giving the ship an impulsive start and then having it move at a constant velocity. In part *a*, the top view of the fin mesh, the fin-tip and trailing-edge vortex systems are represented when no hull is present. In part *c* we show the corresponding front view; in part *e* we show the same but from a different angle. In parts *b*, *d* and *f*, we show the counterparts of parts *a*, *c*, and *e* when the fin is in the presence of an infinite wall. It can be seen that the no-penetration condition on the wall is preserved and that the vorticity shed from the wing tip close to the hull has a tendency to climb up it. In parts *c*, *d*, *e* and *f* one can observe the middle section of the wake being pushed down by the velocity field induced by the fin-tip vorticity. For the case of a ship hull, FINS can consider the fins separated from the hull, similarly as it was shown in Figure 2-11 (for the case of an infinite wall), or attached to

the hull, as shown in Figure 2-12. In such a case the vortex system on the chord fin is eliminated, what speeds up the calculations. In practice we obtained better agreement with experimental results if we considered the fins attached to the hull. On the other hand, the fin-tip vorticity system produced by a fin tip very close to the hull would significantly affected be by the boundary layer in this region. The consideration of such interaction goes beyond the scope of our present work.

Next we consider the influence of the fin-tip vortices. In Figures 2-13 and 2-14 the computed lift coefficients ($C_L$) are given as functions of time. To obtain these results we gave the fin in the presence of the hull an impulsive start; after which we moved it at constant velocity until a steady state evolved. In both cases, the angle of attack is five degrees. In Figure 2-13 the results are for an aspect ratio of two. The calculated $C_L$ that includes the fin-tip vortex system is about 3% larger than the calculated $C_L$ that ignores the fin-tip system. In Figure 2-14, the results are for an aspect ratio of 0.7. Now the calculated $C_L$ that includes the fin-tip system is about 5% larger than the calculated $C_L$ that ignores the fin-tip system. As one would expect, the influence of the tip vortex system increases as the aspect ratio decreases. We note that it takes longer for the steady state to develop for a large aspect ratio. The influence of fin-tip vortices is more noticeable at higher angles of attack. In Figures 2-15 and 2-16, the angle of attack is 10 degrees. For an aspect ratio of two, the increment in $C_L$ is of about 8%; for an aspect ratio of 0.7, the increment in $C_L$ is of about 22%. In Figures 2-13, 2-14, 2-15 and 2-16 the values of $C_L$ corresponding to an impulsive start (time step zero), which are the same for either plot of any figure, are relatively big with respect to the corresponding values of $C_L$ plotted, and they are not shown. We can see from these results that the fin-tip vortex systems are very important for low aspect ratios and high angles of attack. We include these vortex systems in all of the results presented here.

In Figure 2-17 we reproduce some experimental data reported by McCroskey *et al.* [65]. In work related to helicopter aerodynamics, they oscillated a NACA 0012 two-

dimensional airfoil with a simple harmonic motion in pitch around an axis through the one-quarter chord position. The angle of attack is given by

$$\alpha = 3^\circ + 10^\circ \sin(0.2\, t) \tag{2.46}$$

and the chord-base Reynolds number was around $4 \times 10^6$. The flow over the test section of the model was essentially two-dimensional. At various instances, they measured the pressures at 26 locations on the airfoil surface and obtained the loads by numerically integrating the pressure over the surface.

In the top graph the coefficient of lift $C_L$ is given as a function of $\alpha$. Along the broken portion of the curve, the angle of attack is decreasing. The corresponding coefficient of moment $C_M$ is given just below the $C_L$ curve. The hysteresis is obvious. The lift provides negative damping and the moment positive damping. To compare with these results, the present three-dimensional model was transformed into a two-dimensional flat-plate model; the corresponding curves are shown in Figure 2-18. The character of the hysteresis and the peak positive and negative amplitudes for the lift are nearly the same, but the numerical results predict somewhat less aerodynamic damping than what was observed. Also the inclinations of the moment curves are slightly different, but the positive peaks for the moments are nearly the same. The negative peaks differ; the numerical result is larger. The differences in the moments are insignificant since the moments are very small at all times, and LAMP requires the moment about the origin of the *B*-frame, which is completely dominated by the moment of the lift force. For both lift and moment, extreme loads do not occur at the extreme angles of attack in unsteady motion.

The present numerical model can be modified to simulate the flow around thick bodies by placing elements on the actual upper and lower surfaces instead of the mean surface. The numerical results for a thick body are shown in Figure 2-19. The agreement with the experimental data is better; the peak lifts are nearly the same but the hysteresis

is more noticeable than it is for the flat plate and the numerically predicted aerodynamic damping is larger. Both are qualitatively closer to the experimental results. The inclination of the moment curve has shifted slightly.

The experiment of McCroskey *et al*. was done for helicopter's blades. Therefore, the frequency of the oscillations for this experiment are most likely significantly larger than those for a fin attached to the hull of a ship; thus we are testing our model for extreme ranges of operation, and our calculations are still in good agreement with the experimental data.

In Figure 2-20 the numerical results obtained with the present method are compared with some experimental results for steady flow. The normal-force coefficient $C_N$ is plotted as a function of angle of attack for a unit-aspect-ratio, rectangular fin. The numerical values, the experimental results of Scholz [83], and the range of results for three other experiments (Belotserkosvkiy [2], Ermolenko [19] and Winter [99]) are given in the figure. There is some scatter in the experimental results, which were obtained in different wind tunnels with different models. Slight differences in the way the edges are beveled or rounded are enough to produce this scatter. The fin can reach angles of attack of 20 degrees without stall occurring, but most likely cavitation would have occurred in a water tunnel. The nonlinearity of the curve is mostly the result of the fin-tip vortex systems.

Next we compare the results obtained from the present numerical model with the experimental results of Dallinga [16]. In separate tests, he attached two fins with rectangular planforms and different aspect ratios (1.5 and 2.3) to a model of a modern ferry as indicated in Figure 2-21. The fins had symmetric profiles and were relatively thick, 23% nearly twice as thick as the profile test by McCroskey *et al*. [65]. Although most fins have flaps, those used in the experiments did not; moreover, fins are frequently used in conjunction with bilge keels, but none was used in these tests. The chord-based Reynolds number for the tests was $8.7 \times 10^4$ and that for the prototype was $2 \times 10^7$. The numerical model may be viewed as the infinite-Reynolds-number approximation for a

thin fin; hence, the present simulation may estimate the performance of the prototype better than that of the model.

In Figures 2-22 and 2-23 the calculated lift and drag are compared with the observations of Dallinga. In Figure 2-22, $C_L$ is given as a function of the angle of attack. In making the calculations we included the hull of the ship. We estimated the cross section of the hull and the location of the fin using Figure 2-21; we assumed that the hull was cylindrical. The free-surface condition was ignored. The results for the lift shown in Figure 2-22 are in very close agreement over a rather large range of angles of attack, especially if one considers the straight-line, least-squares approximation to the experimental results. At large angles of attack, the freestanding fins generate more lift than the fins attached to the hull because the latter lacks the contribution to the lift due to the fin-tip vortex system that is not shed when the fin is attached to the hull. The calculated flowfields for similar cases were represented schematically in Figure 2-12 for an aspect ratio of 0.8. Surprisingly, the results for the drag, shown in Figure 2-23, are also in good agreement, though not quite as good as in the case of the lift. The broken line shows the numerical predictions when a (constant) residual drag is added to the numerical predictions. We also obtained good agreement with Dallinga's experimental results for a fin of aspect ratio 1.5.

Other comparisons between numerical results obtained from models similar to the present one and experimental results for very low aspect ratio delta wings show excellent agreement even in ground effect separation (see Mook and Nayfeh [70]). The delta wings were operated at high angles of attack and had strong leading edge vortex systems that were responsible for half of the lift.

In Figure 2-24 two plots are shown: 1) the lift produced at different angles of attack $\alpha_i$, and 2) the lift produced when the fin deflection relative to the hull is zero, but the ship is heaving so that the motion-induced angles of attack are the same as $\alpha_i$. The fin is in the presence of a realistic hull [a CG47 cruiser of the US Navy (Figure 2-9)]. As a consequence of the asymmetry introduced by the curvature of the hull, there is a small

difference between the two results. When the fin is in the presence of an ideally infinite straight hull, the plots match perfectly.

Figure 2-25 illustrates the rolling motion reduction obtained when passive fins are present for a beam sea.

## 2.7 Final Remarks

We developed a new general unsteady model of the flowfield around a fin attached to the hull of a ship, called FINS, and a method to combine FINS with such motion-predicting programs as LAMP and FREDYN. In the present examples we used LAMP. LAMP models the hull with a surface distribution of sources whereas the fins are modeled as a vortex lattice in a new program called FINS. Because of the great disparity in the sizes of the ship and the fins, the two interacting codes, LAMP and FINS, use different grid sizes and run with different time steps. Results obtained from LAMP were shown to be in good agreement with experimental data in given previous publications. In numerical examples here, we have shown that FINS predicts forces on the fins in good agreement with experimental data. We showed how the two programs can be used to predict the passive, fin-induced roll damping of a modern cruiser.

In Chapters 5, 8 and 9, we show how to implement nontraditional control strategies to attenuate the roll motion of the ship. There, the accuracy in predicting the general unsteady loads on the fins and hull and the interaction between the LAMP and FINS models are a relevant issues.

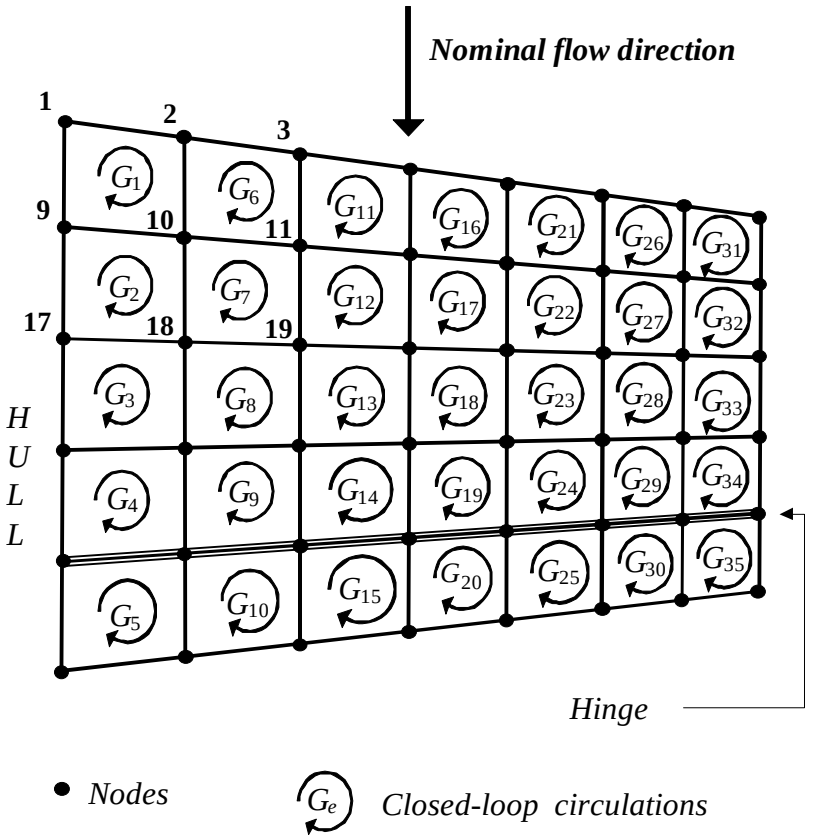


Figure 2-1: Example of a vortex-lattice mesh defined over a fin, and the circulations associated with each element of the mesh.

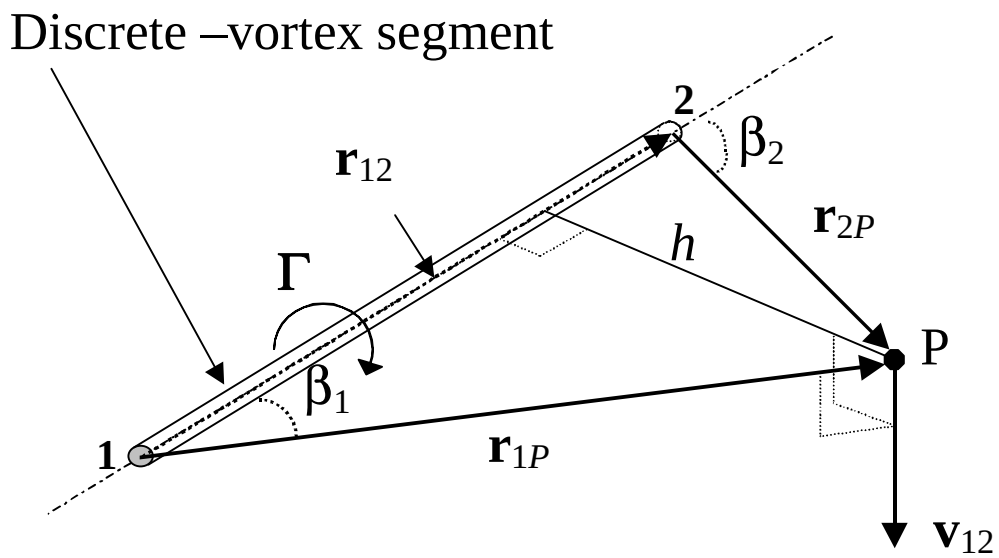


Figure 2-2: Biot-Savart Law. Velocity field associated with a straight segment of vorticity.

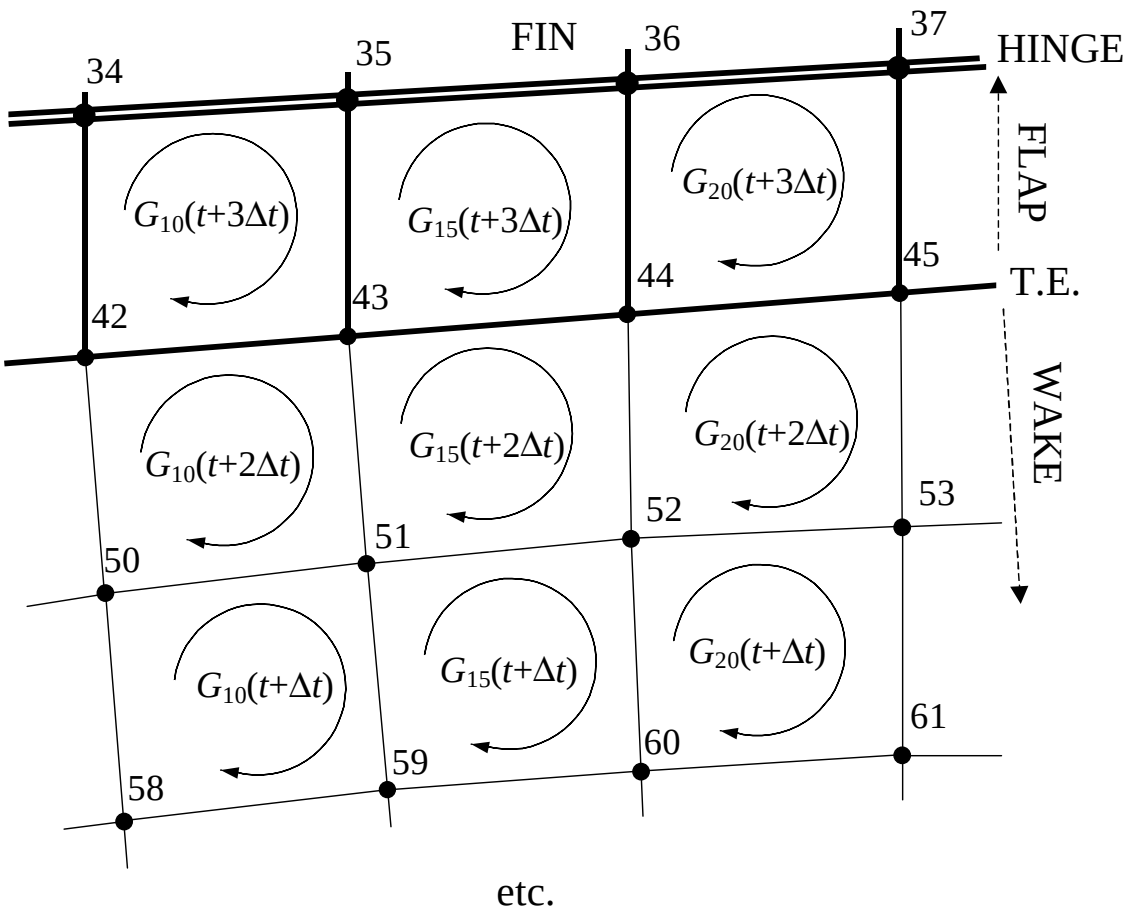


Figure 2-3: Kutta condition: three-dimensional view. Vorticity shed from the trailing edge (T.E.) of an airfoil.

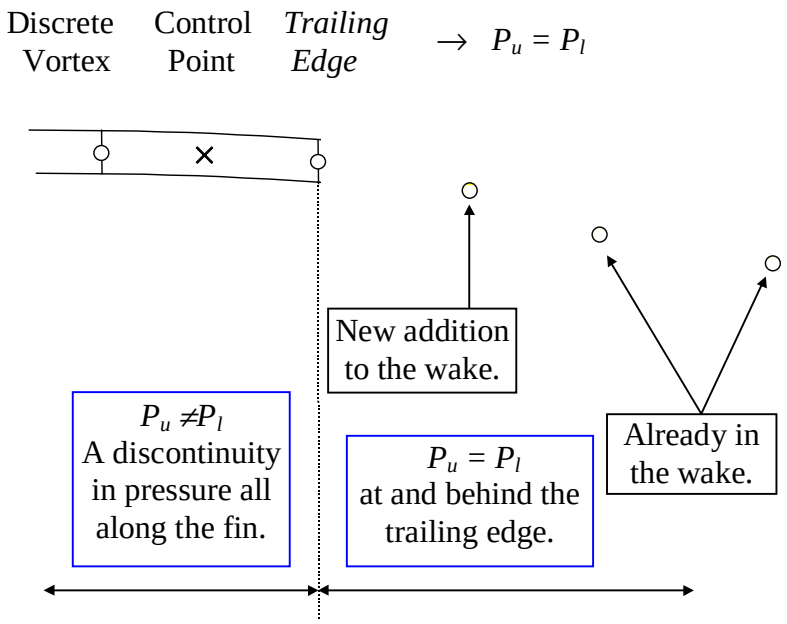


Figure 2-4: Kutta condition: two-dimensional view. Vorticity shed from the trailing edge of an airfoil; $P_u$ is the pressure on the upper surface of the fin and $P_l$ is the pressure on the lower surface of the fin.

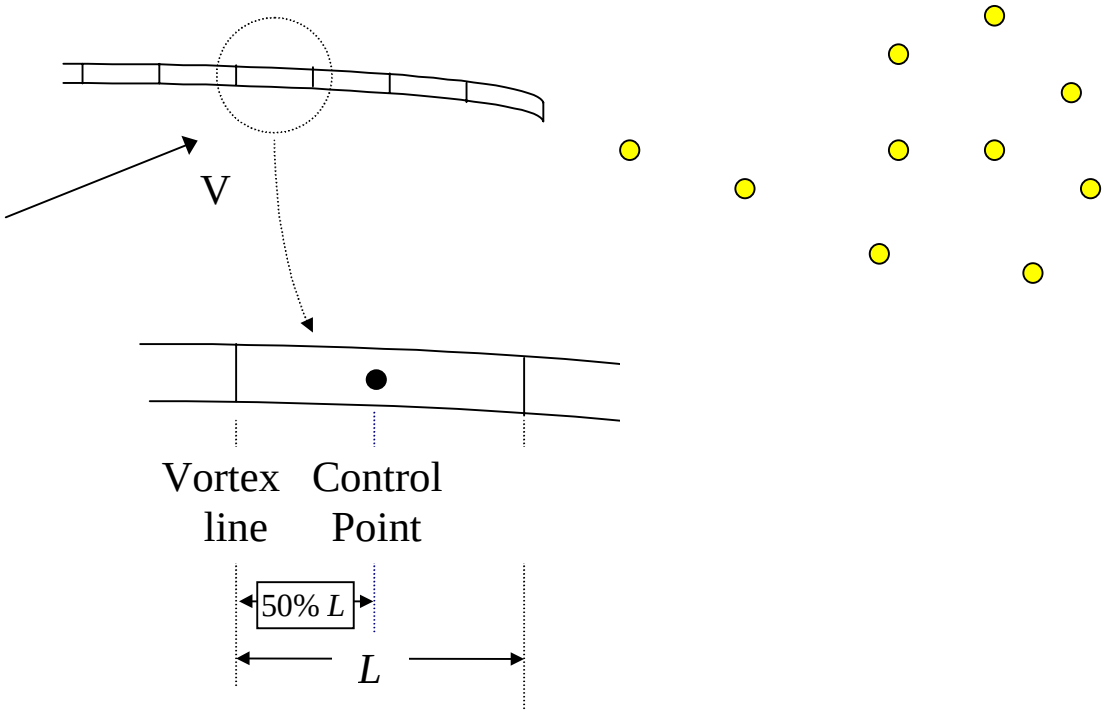


Figure 2-5: Two-dimensional schematic of a vortex sheet.

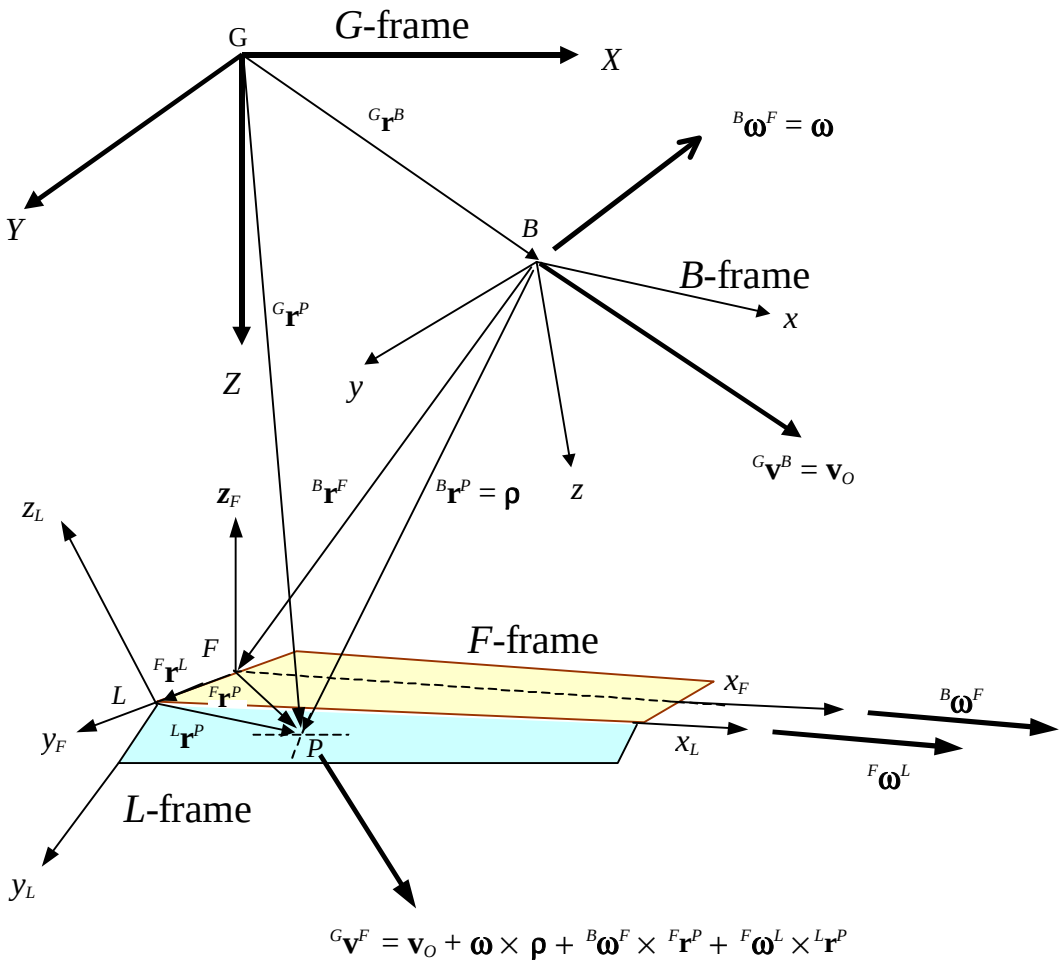


Figure 2-6: Inertial, body-fixed, fin-fixed and flap-fixed reference frames.

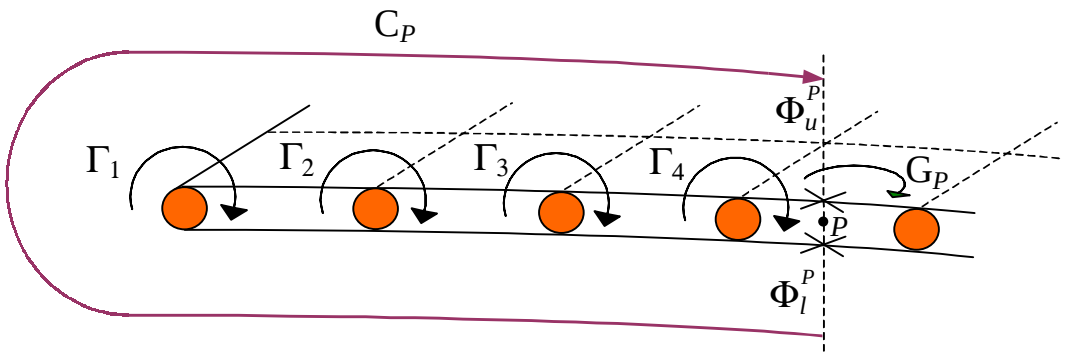


Figure 2-7: A cross section of the vortex sheet (lattice) showing the path of integration, $C_p$, to evaluate $\Phi_u^P - \Phi_l^P$. Shadowed circles represent discrete span-wise vortices; point *P* represents the control point. $G_P = \Gamma_1 + \Gamma_2 + \Gamma_3 + \Gamma_4$ is the circulation for the closed loop of discrete vortex segments enclosing the element that contains the control point.

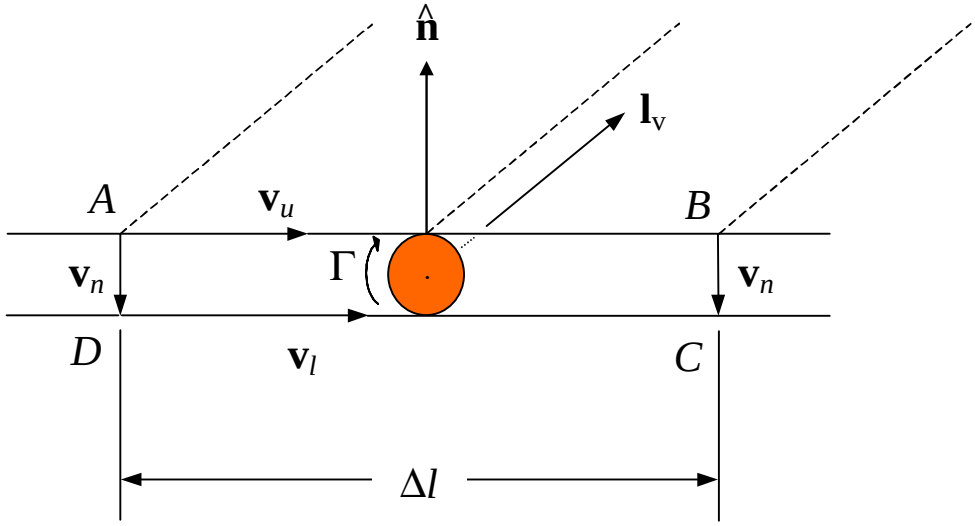


a

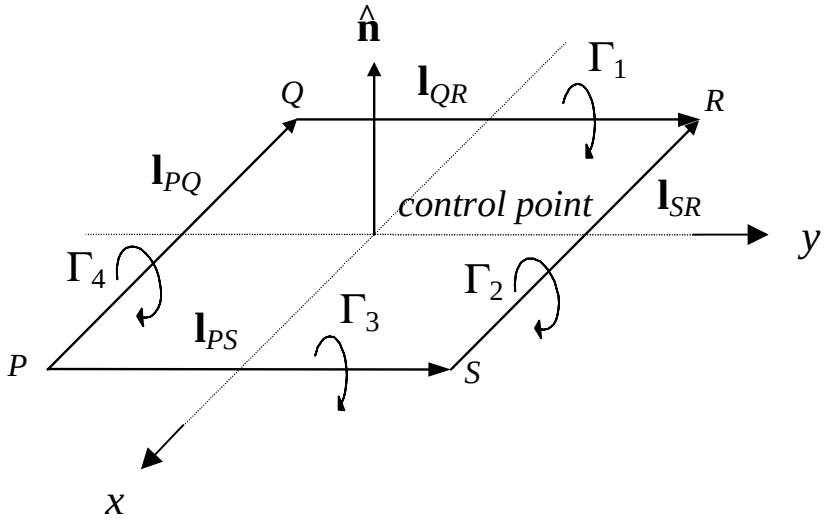


b

Figure 2-8: $\Delta v$ produced by a segment of vorticity between two elements.

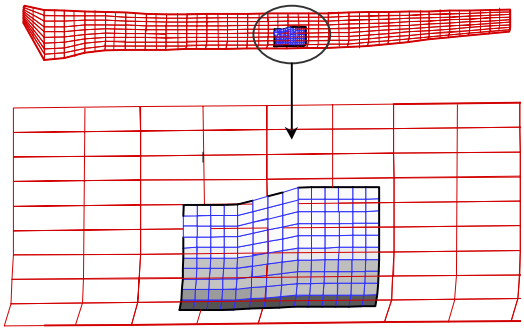

Figure 2-9: Ship and fin grids.

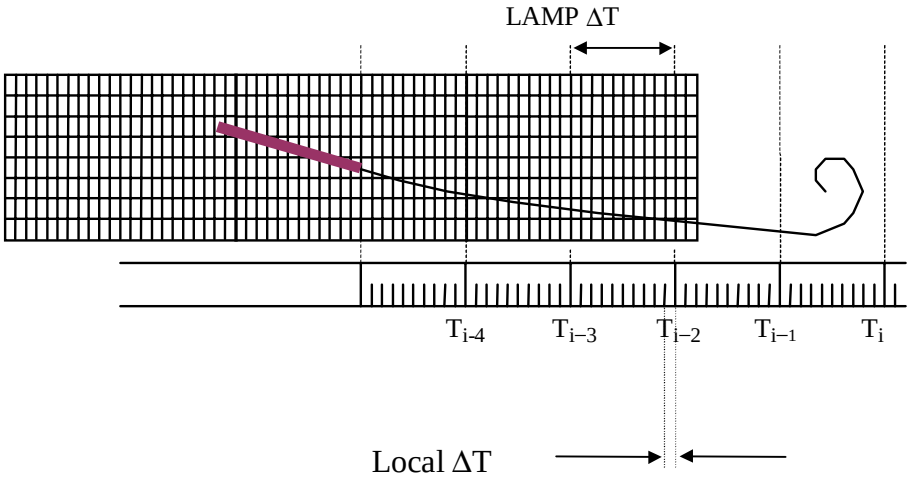


Figure 2-10: Time-marching procedure.

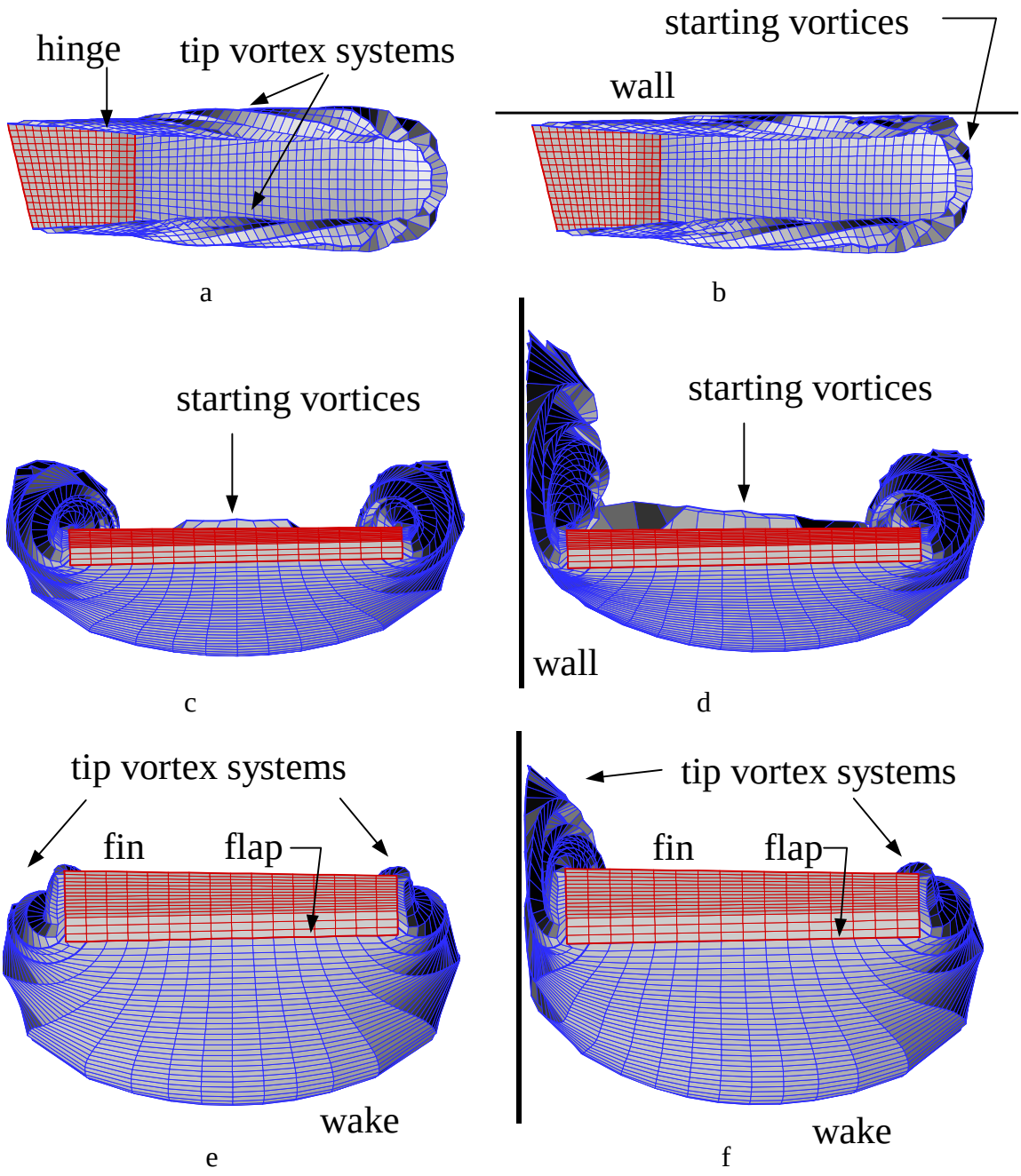


Figure 2-11: Fin mesh and vorticity in a free flow and in the presence of an infinite wall. Number of fin elements = 256. Aspect ratio = 0.8. Fin deflection = 10 degrees. Flap deflection = 10 degrees.

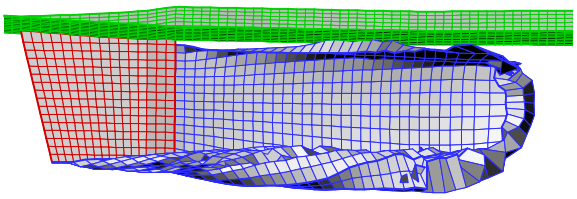

a

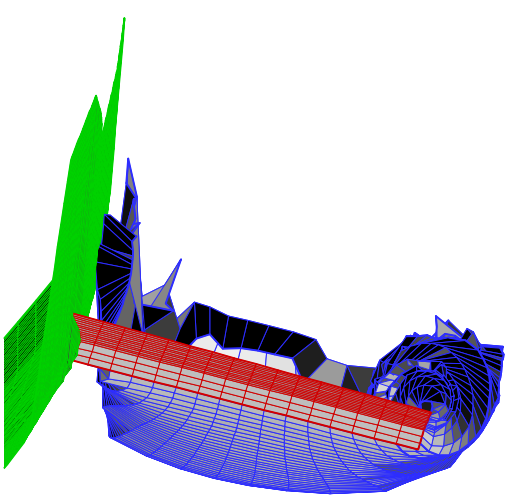

b

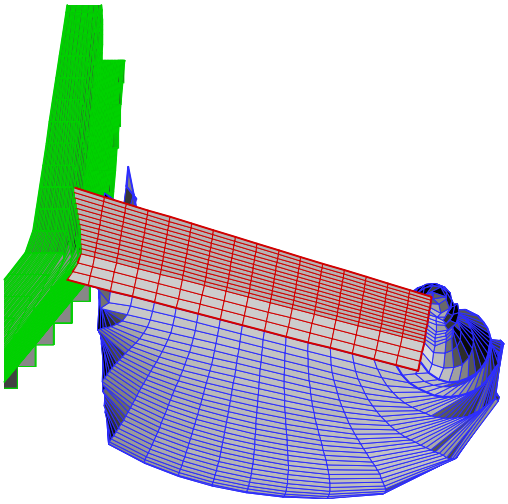

c

Figure 2-12: Top (a) and front views (b, c) of a fin mesh and vorticity of a fin attached to the hull. Number of fin elements = 256. Aspect ratio = 0.8. Fin deflection = 10 degrees. Flap deflection = 10 degrees. Dihedral angle = 14 degrees.

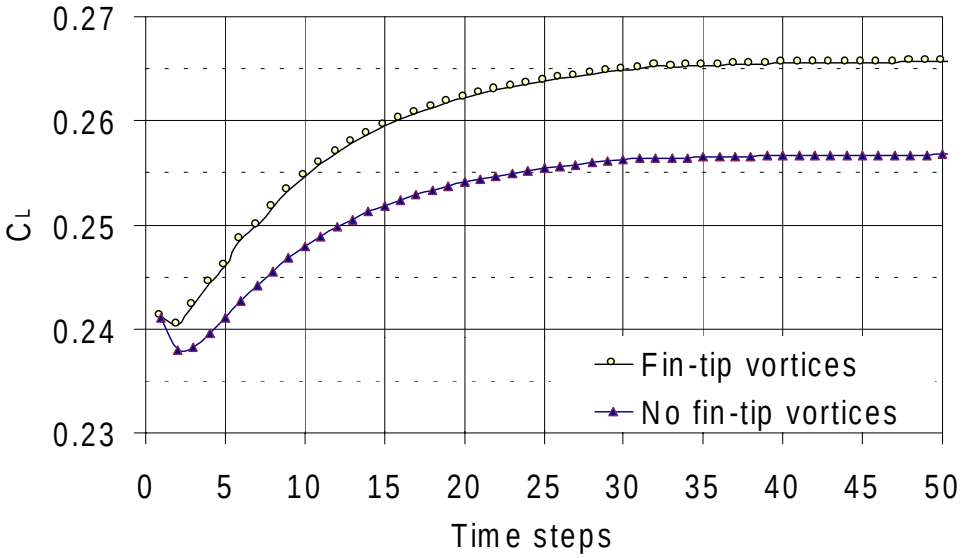


Figure 2-13: $C_L$ computations with and without the fin-tip influence, for a fin of aspect Ratio 2 at an angle of attack of 5 degrees.

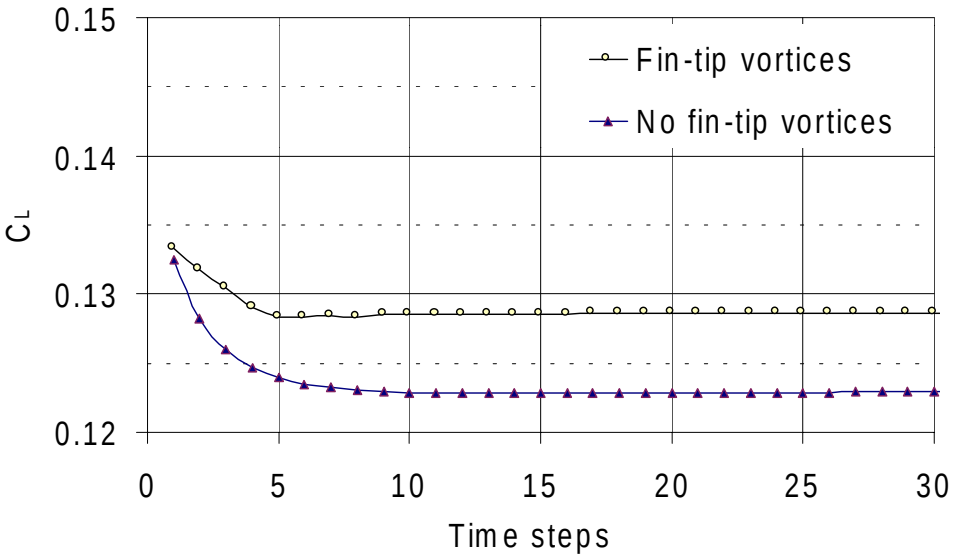


Figure 2-14: $C_L$ computations with and without the fin-tip influence, for a fin of aspect ratio 0.7 at an angle of attack of 5 degrees.

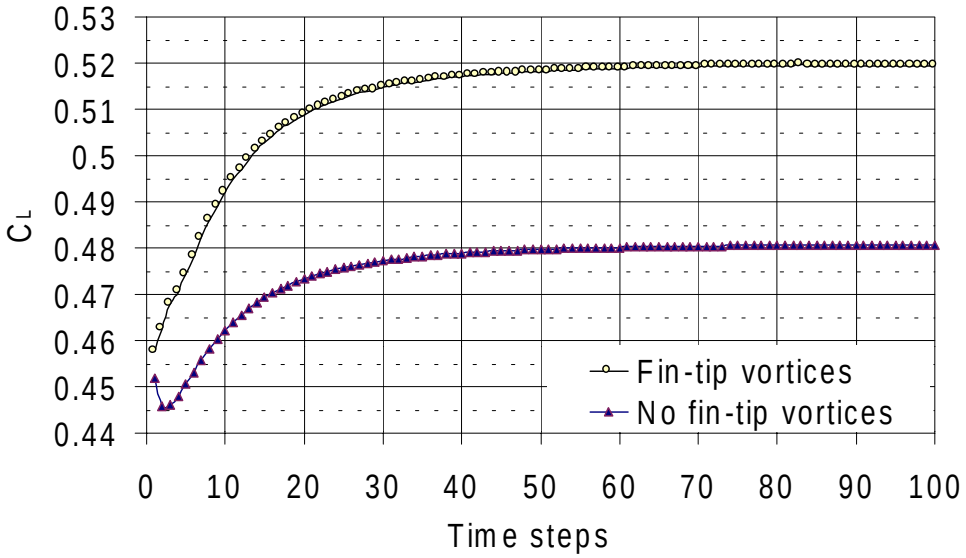


Figure 2-15: $C_L$ computations with and without the fin-tip influence, for a fin of aspect ratio 2 at an angle of attack of 10 degrees.

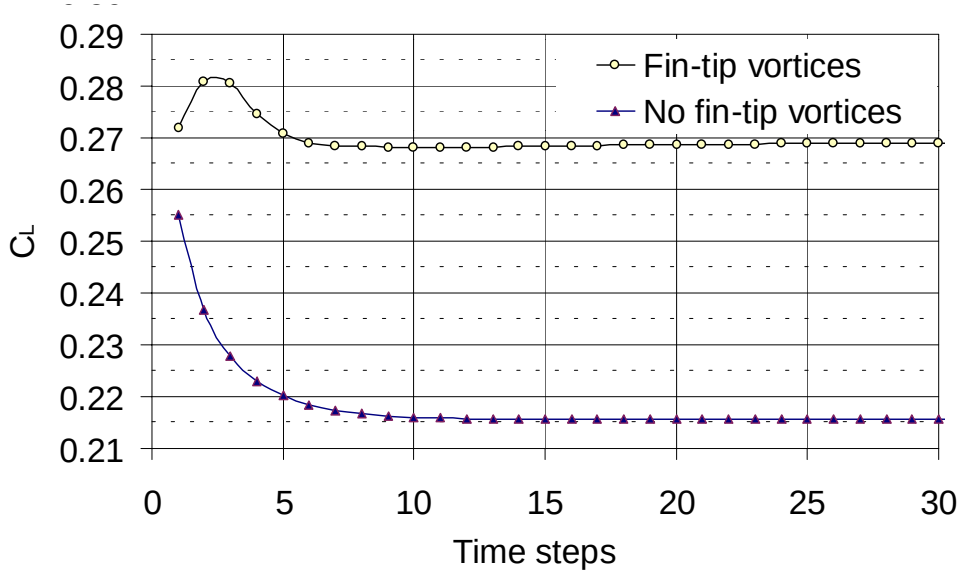


Figure 2-16: $C_L$ computations with and without the fin-tip influence, for a fin of aspect ratio 0.7 at an angle of attack of 10 degrees.

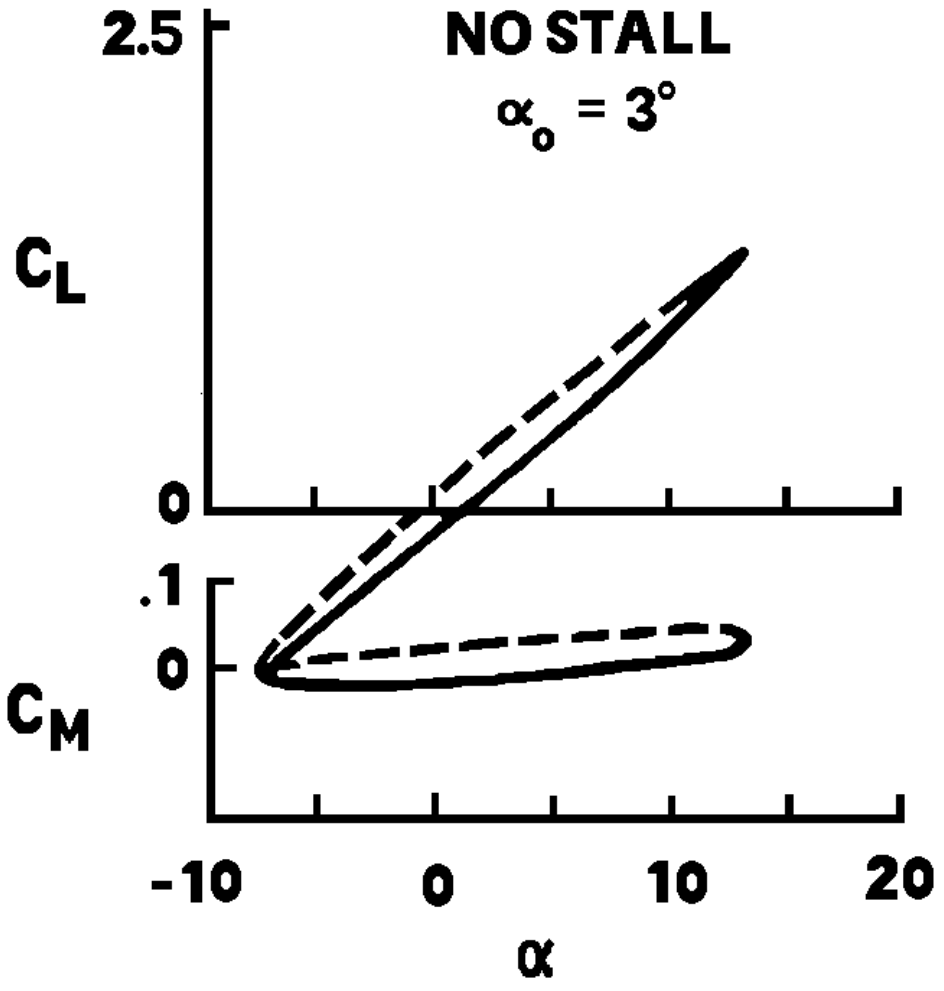


Figure 2-17: The experimentally obtained variation of unsteady aerodynamic loads with angle attack for the NACA 0012. $M_\infty = 0.3$, chord-based $Re = 4 \times 10^6$, $\alpha = 3^\circ + 10^\circ \sin(0.2\,t)$, and solid lines denote increasing α. (Taken from McCroskey *et al.* [65]).

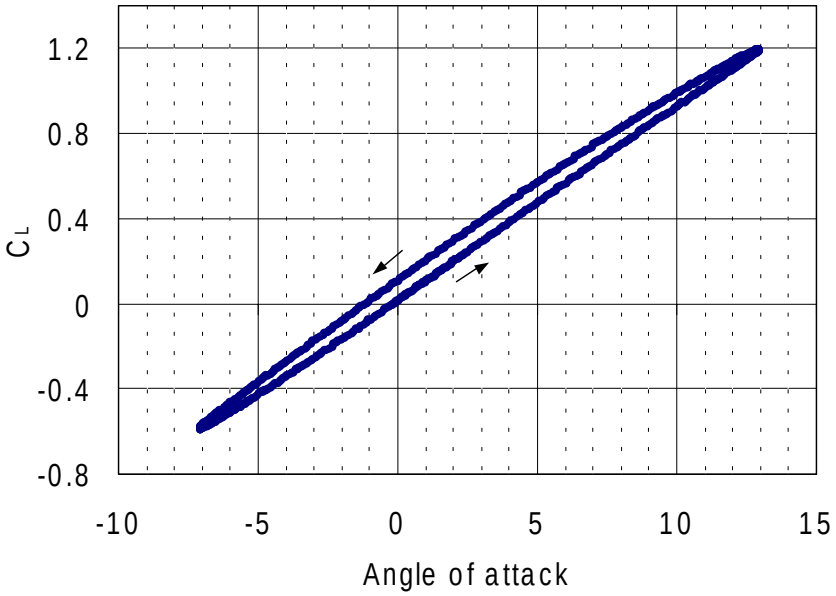


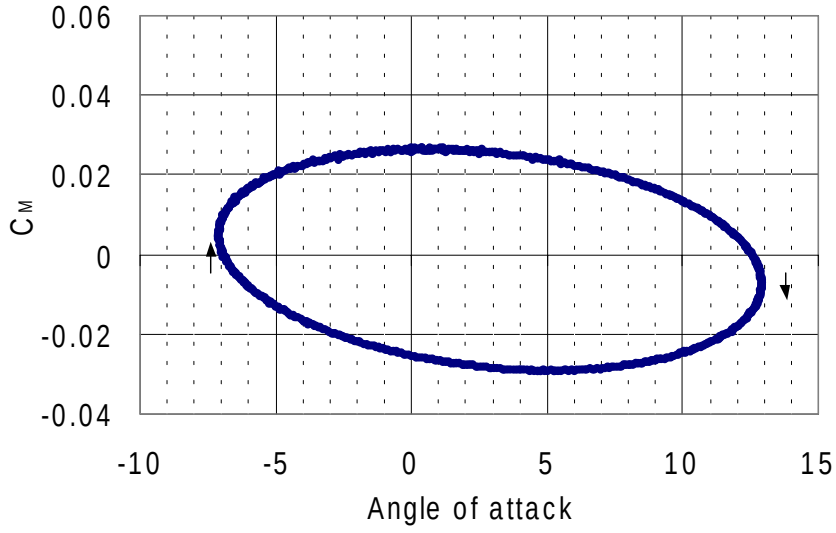


Figure 2-18: The computed variation of unsteady aerodynamic loads with angle of attack for a flat plate of infinite aspect ratio; $\alpha = 3^\circ + 10^\circ \sin(0.2\,t)$.

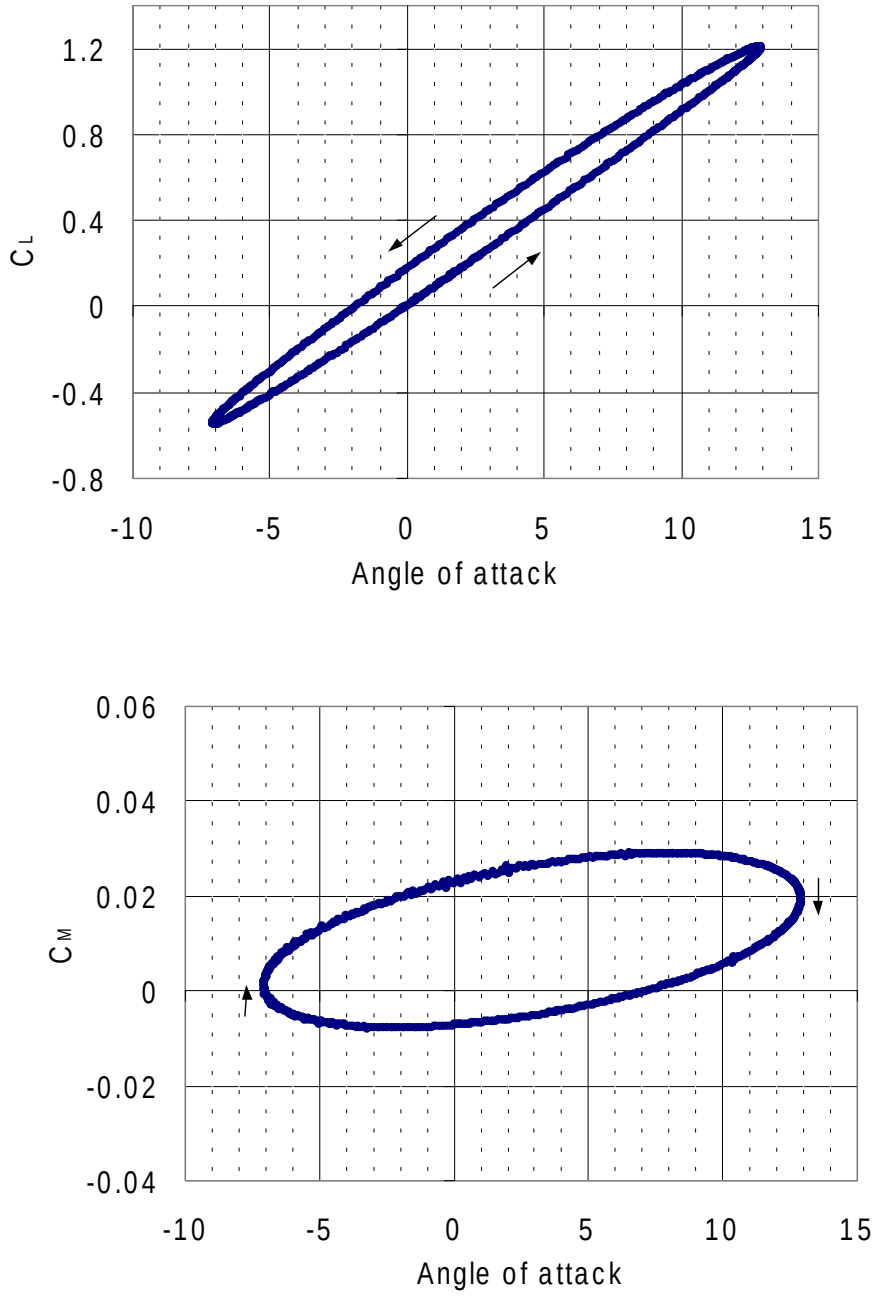


Figure 2-19: The computed variation of unsteady aerodynamic loads with angle of attack for a NACA 0012 airfoil; $\alpha = 3^\circ + 10^\circ \sin(0.2\,t)$.

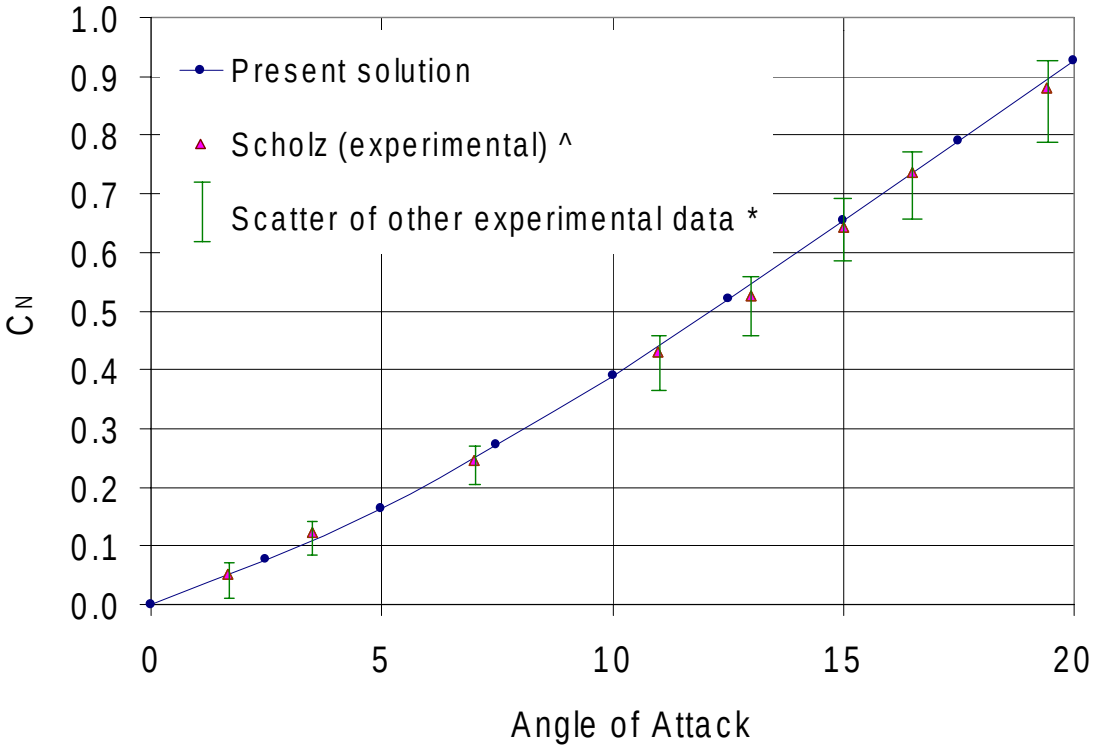


Figure 2-20: A comparison of the numerical and experimental normal-force coefficients as functions of the angle of attack for a rectangular, unit-aspect-ratio fin in a steady airstream. (^ Scholz [83], * Belotserkosvkiy [2], * Ermolenko [19] and * Winter [99] experimental data).

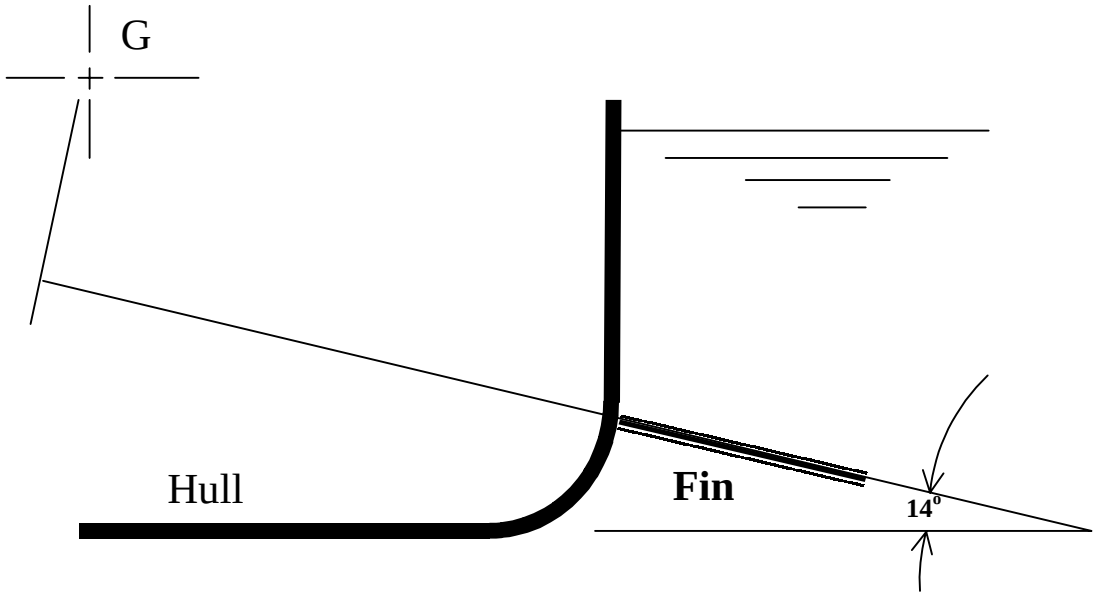


Figure 2-21: Schematic representation of Dallinga's model. (Taken from Dallinga [16]).

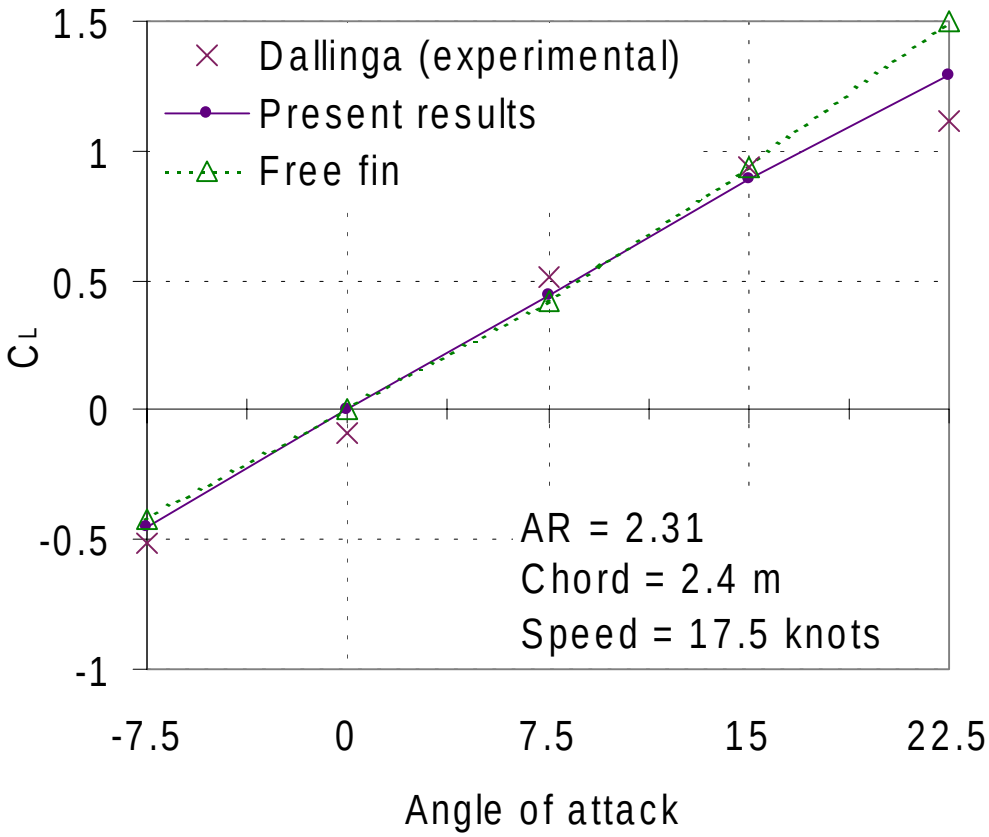


Figure 2-22: Comparison of numerical and experimental lift coefficients. (Experimental data from Dallinga [16]).

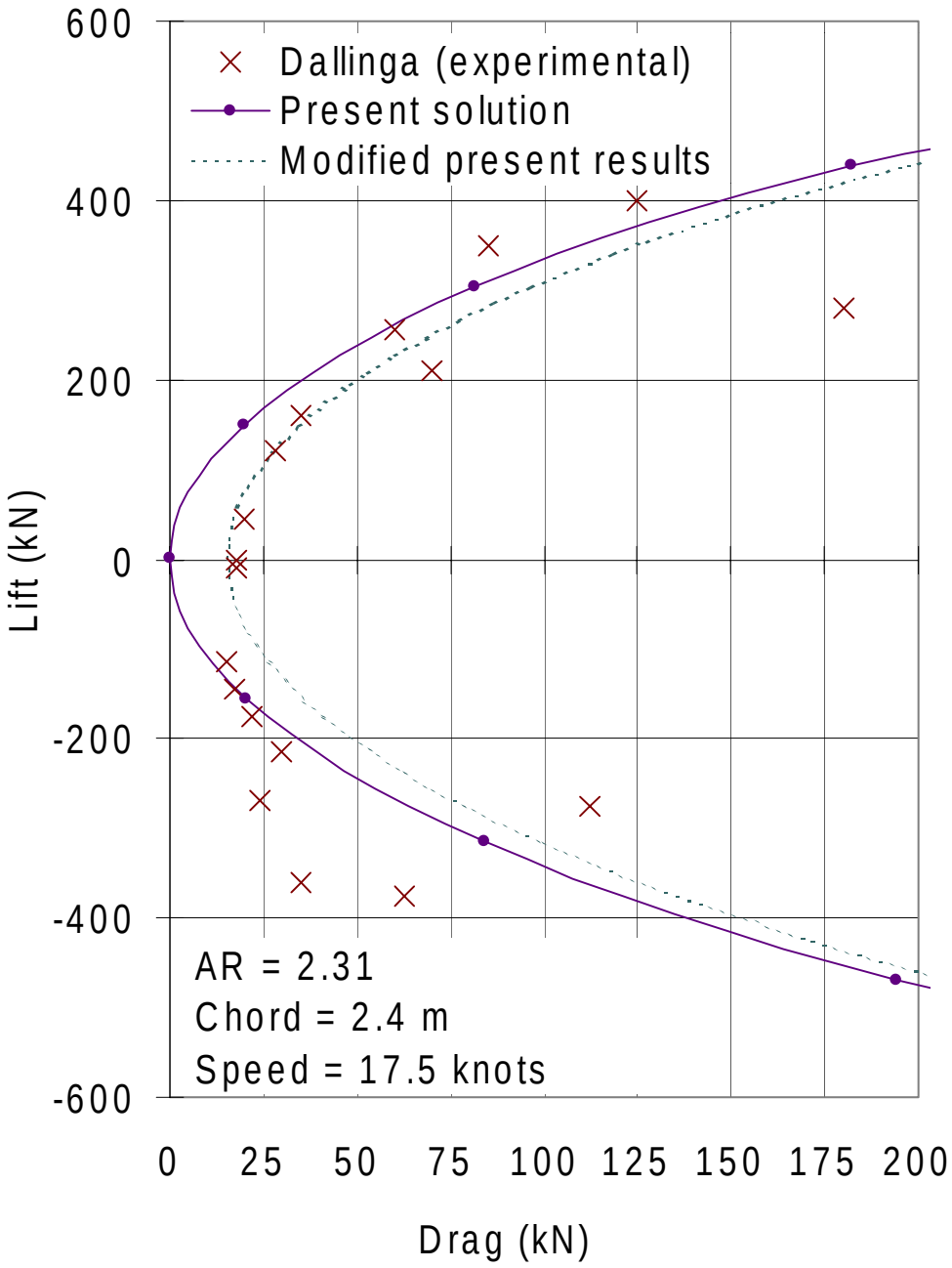


Figure 2-23: Comparison of numerical and experimental drag polars (Experimental data from Dallinga [16]).

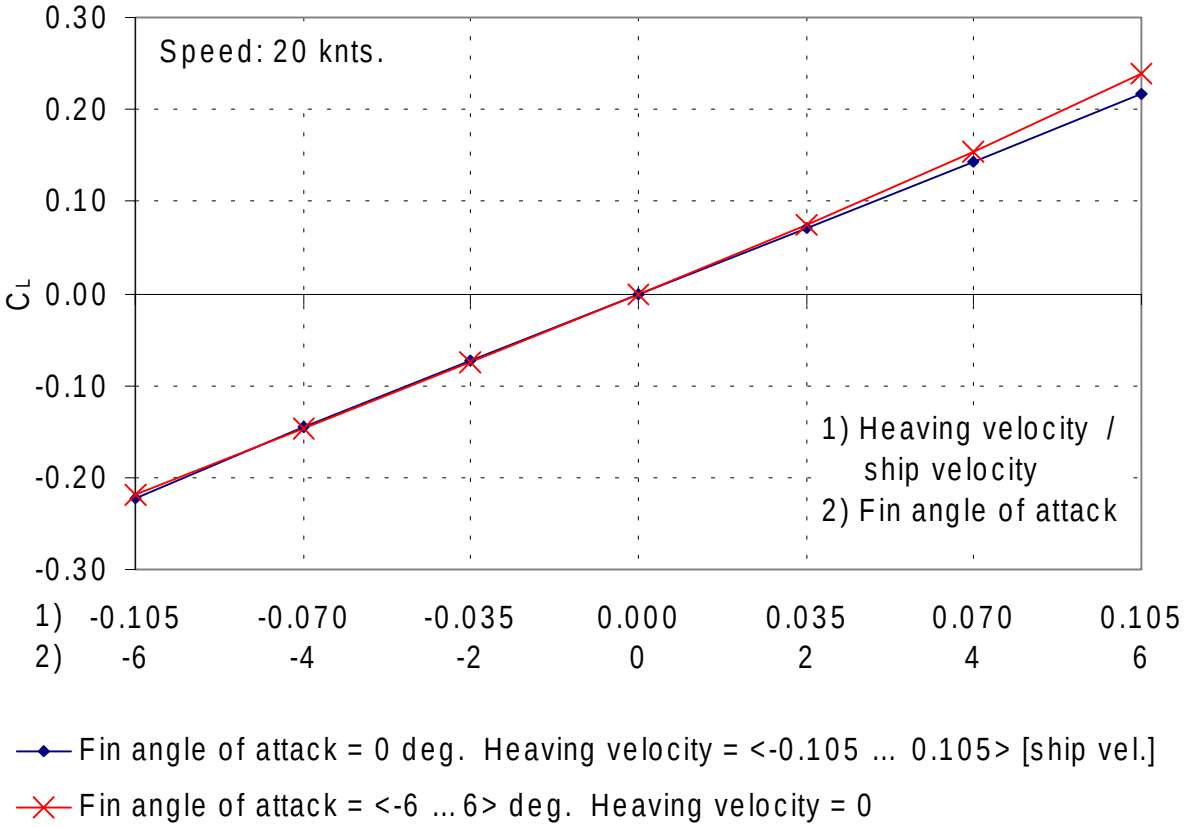


Figure 2-24: (1) Heaving-induced lift with zero fin angle of attack, and (2) lift as a function of fin angle of attack with no heaving motion. The fins are attached to the (curved) hull of a CG47 cruiser.

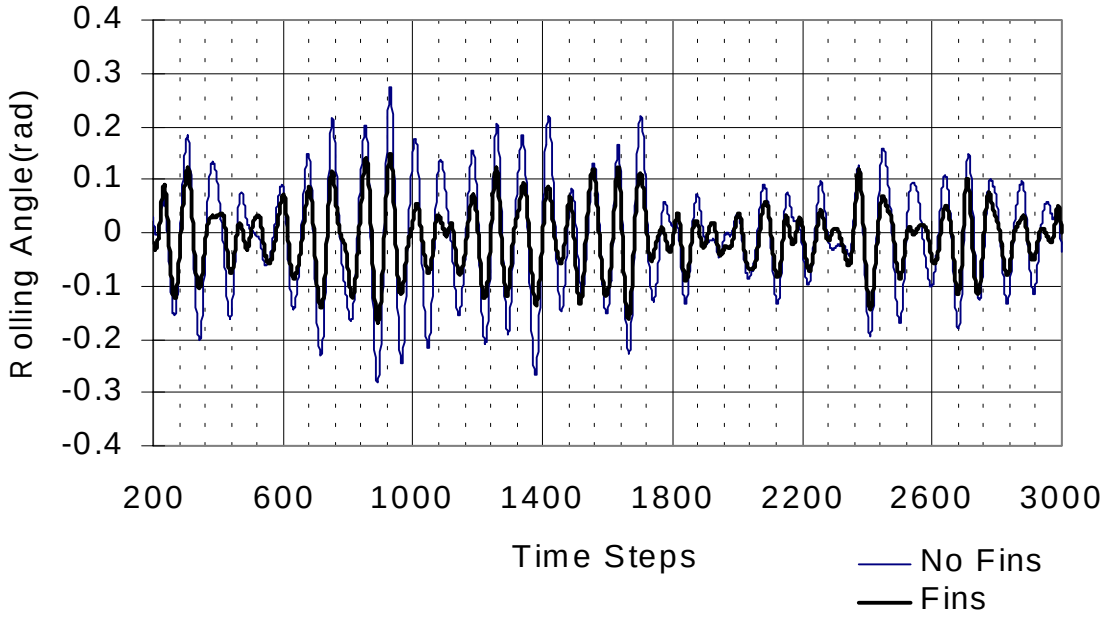


Figure 2-25: Rolling motion for a beam sea. Speed 20 knots. Thin line: no fins are present. Thick line: fins are present.

Table 2-1: Time-marching procedure.

*CALL from LAMP*

*IF* LAMP Time == 0 *THEN*

*Perform FINS Initializations
*Compute FINS time steps (FTP) per each LAMP time step:

$$\text{FTP} = \text{Integer}\left(\frac{LAMP\ \Delta T}{FIN\ \Delta T} + 0.5\right)$$

*Solve for circulations

*ENDIF*

*IF* Same LAMP Time Step *THEN*
*LAMP is iterating →predictor-corrector*

*Use original wake position distribution for current LAMP time step.

*ELSE IF* New LAMP Time Step *THEN*
*LAMP has finished iterating*

*Go ahead from last computed wake data.
*Save present wake data before starting new computations.

*ENDIF*

*IF* LAMP Time > 0 *THEN*

*DO* N == 1 *TO* FTP
* Convect the wake
* Move the fin
* Solve for circulations
* FIN *Time* = FIN *Time* + FIN *ΔT*
*END DO*

*ENDIF*

* Compute pressures and loads
* Call Control Routine
* Call Training Routine
* Save current FINS data

* *RETURN* to LAMP